Available online at www.sciencedirect.com
ScienceDirect
Journal of Magnetic Resonance 190 (2008) 7–25
JMR Journal of Magnetic Resonance
www.elsevier.com/locate/jmr

A paramagnetic molecular voltmeter

Jack T. Surek *, David D. Thomas

Department of Biochemistry, University of Minnesota Medical School, Jackson Hall 6-155, 321 Church Street SE, Minneapolis, MN 55455, USA

Received 22 March 2007; revised 20 July 2007
Available online 5 October 2007

Abstract

We have developed a general electron paramagnetic resonance (EPR) method to measure electrostatic potential at spin labels on proteins to millivolt accuracy. Electrostatic potential is fundamental to energy-transducing proteins like myosin, because molecular energy storage and retrieval is primarily electrostatic. Quantitative analysis of protein electrostatics demands a site-specific spectroscopic method sensitive to millivolt changes. Previous electrostatic potential studies on macromolecules fell short in sensitivity, accuracy and/or specificity. Our approach uses fast-relaxing charged and neutral paramagnetic relaxation agents (PRAs) to increase nitroxide spin label relaxation rate solely through collisional spin exchange. These PRAs were calibrated in experiments on small nitroxides of known structure and charge to account for differences in their relaxation efficiency. Nitroxide longitudinal (R_1) and transverse (R_2) relaxation rates were separated by applying lineshape analysis to progressive saturation spectra. The ratio of measured R_1 increases for each pair of charged and neutral PRAs measures the shift in local PRA concentration due to electrostatic potential. Voltage at the spin label is then calculated using the Boltzmann equation. Measured voltages for two small charged nitroxides agree with Debye–Hückel calculations. Voltage for spin-labeled myosin fragment S1 also agrees with calculation based on the pK shift of the reacted cysteine.

Keywords: EPR; Accessibility; Electrostatics; Paramagnetic relaxation; Transition metal complex

1. Introduction

1.1. Importance of protein electrostatics

Electrostatics is fundamental to protein structure, dynamics, interactions and function [1,2]. In particular, proteins that mediate energy or signal transduction must transmit electrostatic energy from substrate hydrolysis [3] or ligand binding [4,5] across their structures. In myosin, for example, the release of ATP hydrolysis energy results in conformational changes over distances of 5 nm or more [6], which involve torsional and translational movements of specific alpha helices of the myosin head [7]. These interorbital forces are electrostatic [8,9] and generate highly localized potentials. To date, protein spectroscopy has focused on *describing* changes in structure and dynamics generated primarily by these electrostatic forces. In the present study, we develop a method to measure these electrostatic forces quantitatively, as a step toward *explaining* the observed structural changes.

1.2. Dynamic range and sensitivity needed

What is the magnitude of electrostatic potential change that must be measured? One estimate comes from sidechain ionization, which is typically within one pK unit [10–12], corresponding to ±59 mV for a single charge ionization at 25 °C, based on the Tanford–Roxby equation [13]. The SH1 cysteine of myosin S1 has an unusually large pK shift of 2.27, corresponding to +135 mV [14,15], which we use later. Another estimate comes from the energetics of ATP hydrolysis, where 7.3 kcal/mol in energy is liberated with a loss of 1 electron charge, corresponding to a 300 mV potential change. Assuming 50% efficiency, this suggests that a fully general method should measure potentials over a range of ±150 mV. In most cases probes will be remote

* Corresponding author. Fax: +1 612 624 0632.
E-mail address: jts@ddt.biochem.umn.edu (J.T. Surek).

1090-7807/$ - see front matter © 2007 Elsevier Inc. All rights reserved.
doi:10.1016/j.jmr.2007.09.020

from such centers, so they must discern small changes with millivolt precision.

1.3. Calculating electrostatic potential from high-resolution structure

In principle, structures obtained from X-ray crystallography or NMR can be used to calculate the electrostatic potential at any point within the molecule, using the Poisson–Boltzmann equation. However, the uncertainty of these calculations has been estimated to be about 40 mV in proteins [2,16,17]. Furthermore, crystal-trapped structures can differ significantly from solution structures, which are likely to be less ordered and more dynamic, especially in energy-transducing proteins [18,19]. When available, an ensemble of NMR solution structures can give a more accurate computational voltage than that derived from an X-ray crystal structure [20]. Some of the most critical conformational states are transient or flexible and are thus not easily trapped in crystals [21,22], and most supramolecular assemblies (e.g., actomyosin) have not been crystallized and are too large for high-resolution NMR analysis. There is clearly a need for a general method that measures electrostatic potential accurately in solution under functional conditions. Also, electrostatic modeling programs such as DelPhi and APBS are geared toward the calculation of relatively large potential distributions produced by surface charges, not the highly localized potential distributions that report energy transmission through proteins. Collisional spin exchange offers the prospect of measuring these potentials directly, going beyond these current limitations.

1.4. Site-directed probe techniques

Site-directed mutagenesis, usually producing single-cysteine mutants, is the most general method of obtaining site-specific structural information in solution. Electrostatic potentials have been estimated using cysteine reactivity to charged reagents [4,23], but this has low time resolution and these reactions can involve many influences. Cysteine p*K* shift on a protein surface can be measured potentiometrically [14], but ionization can also depend on hydrogen bonding and hydrophobic interactions in addition to electrostatic potential [24]. Also, this method requires varying pH, a variable often important to biochemical state. Hydrogen exchange has been used to estimate the electrostatic potential near metal binding sites in proteins, but is limited to proteins with metal centers and sensitive to electrostatic potentials of ~ 20 mV and above [10].

A more promising approach involves spectroscopic measurements of the accessibility of charged relaxation agents to a site-directed probe. Electrostatic forces perturb local agent concentration, so changes in probe relaxation rate are related to the local voltage through the Boltzmann equation. For example, collisional fluorescence quenching [25–27] and diffusion-enhanced resonance energy transfer [27–34], using charged relaxation agents in solution, provide direct spectroscopic measurements of electrostatic potential at specific probe sites. In most cases, the large optical probes required limit spatial resolution and can disrupt protein function, and the ns lifetimes of most fluorescent probes require the addition of high concentrations of relaxation agent (>100 mm), which can disrupt protein structure and function. NMR has been used to make electrostatic measurements on proteins, using charged nitroxides as relaxation agents [35,36], but these measurements are spatially averaged because they are dominated by long-distance dipolar relaxation. NMR signals are also 700 times smaller than those of EPR, making NMR less sensitive to small voltages [35].

EPR accessibility experiments that emphasize electrostatics have been performed previously [16,17,37–42], but studies that actually measured electrostatic potentials at nitroxide spin labels, utilizing paramagnetic relaxation agents (PRAs) form a smaller set [16,17,40,42,43]. Shin and Hubbell made pioneering measurements using electron–electron double resonance (ELDOR) with charged and neutral ^{15}N nitroxides as PRAs against ^{14}N nitroxide labels [16,17]. They estimated an electrostatic potential at the surface of a charged lipid membrane by fitting measured values of R_1 from ELDOR as ionic strength was varied, and they found agreement with a previously estimated value. However, neither the ^{15}N nitroxide PRAs nor the instrumentation for ELDOR measurements is commonly available, and ELDOR is an indirect measure of accessibility because it relies on perturbing the cross-coupling between ^{14}N nuclear states with slowly relaxing PRAs [44,45,42]. Also, when they measured the more localized electrostatic potential at a spin label intercalated in DNA, it was 14% of the value expected based on modeling. This underestimate may be due in part to the slow (μs) R_1 relaxation time of nitroxide PRAs, resulting in measurement of a spatial average of the potential distribution.

Electrostatic potentials at nitroxide spin labels on phospholipase A_2, complexed over a charged lipid membrane, have been measured from increases in R_2 with the addition of chromium oxalate (CrOx aka $Cr(C_2O_4)_3^{3-}$) as a PRA [40,43]. These measurements are important precursors to ours, but absolute accuracy remains unknown primarily because they remain based on measurements over a large complex system (charged membrane) having a large uniform electrostatic potential distribution. Calibrations are needed on small molecules carrying single charges to ensure that relaxation agents do indeed operate collisionally to measure localized potential distributions. There is also a need to account for differences in steric accessibility between labeling sites.

In the present study, we use PRA's with ps relaxation times to ensure that the relaxation enhancement is due entirely to collisional spin exchange [46], and we use small nitroxide spin labels of known structure and charge to calibrate these for accurate voltage measurements. Saturation recovery EPR, using pulsed excitation and detection, is a viable alternative to conventional EPR for accessibility mea-

surements [47,48], but the present study uses the more widely available conventional EPR technology. We perform these EPR experiments on a set of PRAs which encompass all charge states (−, 0, +). The PRA spin-exchange rate is proportional to the collision rate, and this is proportional to local concentration. We employ the Boltzmann equation to estimate electrostatic potential from the shift in charged PRA concentration relative to bulk as observed through relaxation due to spin exchange. Finally, we apply the method to spin-labeled myosin to show that it can measure small electrostatic potentials on proteins with an accuracy of a few mV.

2. Methods

2.1. Spin exchange as a bimolecular chemical reaction

Collisional spin exchange can be described through the kinetics of a bimolecular reaction:

$$NO^* + PRA \underset{k_{-1}}{\overset{k_1}{\rightleftarrows}} NO^*PRA \xrightarrow{k_2} NO + PRA^* \tag{1}$$

Solving this equation leads to the expression for the spin exchange reaction rate:

$$W_{ex} = \frac{1}{[NO^*]}\frac{d[NO]}{dt} = \frac{k_1 k_2 [PRA]_{NO}}{k_{-1} + k_2} = k_e [PRA]_{NO}. \tag{2}$$

PRA concentration bears the subscript "NO" to emphasize that it is sampled at the nitroxyl group. We selected PRAs with spin-lattice relaxation rates R_1 ($1/T_1$) much greater than the nitroxide resonance frequency to eliminate dipolar relaxation [46] and show that it is insignificant by calculations done in the Section 4. So collisional spin exchange is the only mechanism that increases R_1 in our measurement system as given by

$$\Delta R_1 = W_{ex} = k_e [PRA]_{NO}. \tag{3}$$

Assuming that local PRA concentration is governed by the electrostatic potential of the nitroxyl electron, Eq. (3) indicates that spin exchange rate k_e is directly measurable when it is neutral, or known. Strong collisional spin exchange ($k_2 \gg k_{-1}$ in Eqs. (1), (2)), is diffusion-controlled with $k_e = k_1 \approx 3.6$ MHz/mM for idelized collisions in water at 25 °C, p154 in [49]. For real PRA-nitroxide collisions, k_e is smaller due to electronic, steric, and magnetic factors [49]. For example $k_e \approx 0.2\ k_1$ was measured for $Fe(CN)_6^{3-}$ in aqueous solution with a nitroxide spin label [50]. We determine k_e directly from changes in R_1 for each PRA by measuring spin exchange rates against small nitroxides of known structure and charge (described below). For spin labels on proteins k_e is further reduced by steric accessibility.

2.2. Calculating voltage from relaxation enhancement

The concentration of PRA with charge Z at r, [PRA](r), due to electrostatic potential $V(r)$ is related to the bulk solution concentration $[PRA]_\infty$ through the Boltzmann equation [2,16,17,38,40,42]

$$[PRA](r) = [PRA]_\infty \exp\left\{-\frac{ZF[V(r)]}{RT}\right\}, \tag{4}$$

where F is the Faraday constant, R is the gas constant and T is temperature. Here we assume an electrostatic potential of mean force [51] acting on each PRA and that any short range forces act to change PRA k_e values (Eq. (3)). The two relevant short-range forces are steric Van der Waals forces and nitroxyl group hydration. We select small PRAs of the same diameter, to ensure that their k_e values are lowered by the same amount in collisions with a spin label in a tight protein crevice. Nitroxyl group hydration has been hypothesized to explain nitroxide–nitroxide k_e values that are half as large in aqueous compared to organic solutions [49]. We later account for this water by defining the nitroxyl oxygen surface from which position r in Eq. (4) is set. The key concept of this calibration is that while PRA k_e values may vary between experiments, their ratios between such PRAs remain the same, allowing constant correction factors to be defined in Eq. (6).

Relaxivity χ is calculated by combining Eqs. (3) and (4) [38]:

$$\chi_1 \equiv \frac{\Delta R_1}{[PRA]_\infty} = k_e \exp\left(\frac{-ZFV}{RT}\right) \tag{5}$$

There is a similar equation for χ_2, but our primary interest is χ_1. Thus when the nitroxyl oxygen resides in a neutral electrostatic potential ($V = 0$), relaxivity χ is the second-order rate constant k_e unique to each PRA (Eq. (3)). We calibrated three PRAs of positive, negative and neutral charge (Section 2.1) against charged and ionically neutral small nitroxides by measuring their relaxivities in aqueous buffer to derive calibration factors K_1 for each charged PRA with respect to the neutral:

$$K_1^+ \equiv \frac{\chi_1^+(V=0)}{\chi_1^0(V=0)} = \frac{k_e^+}{k_e^0} \quad K_1^- \equiv \frac{\chi_1^-(V=0)}{\chi_1^0(V=0)} = \frac{k_e^-}{k_e^0}. \tag{6}$$

The + and − superscripts denote PRA charge state. The potential at a nitroxide is then calculated by combining Eqs. (5) and (6):

$$V^+ = \frac{-RT}{Z^+F}\ln\left[\frac{\chi_1^+}{\chi_1^0 K_1^+}\right] \quad V^- = \frac{-RT}{Z^-F}\ln\left[\frac{\chi_1^-}{\chi_1^0 K_1^-}\right] \tag{7}$$

Here charge values $Z^{+/-}$ carry sign and $RT/F = 25.68$ mV at 25 °C. If both charged PRAs sensed their concentration at the same r then these voltages would agree. The r values for our charged PRAs differ by several angstroms. Once the calibration is established, Eq. (7) is used to determine voltage, usually with relaxivities χ_1 replaced by changes in R_1, measured by adding charged and neutral PRAs at the same concentration.

2.3. Selecting PRAs for an EPR voltmeter

To measure electrostatic potential through collisional spin exchange, we chose the PRAs in Fig. 1. These have comparable small diameters and magnetic properties, are stable in aqueous solution, and are either commonly available or easily made. The selected PRAs have spin-lattice relaxation rates $R_1 > 100$ GHz, (Table 4). Because these rates are substantially above the nitroxide resonance frequency, relaxation through dipolar coupling is insignificant, leaving only relaxation through collisional spin exchange. This relaxation rate is also fast compared with the intermolecular collision frequency for the small nitroxides tested here at 0.5 mM. So PRA addition does not cause cross-coupling between different nuclear spin states of the ^{14}N nitroxide [49,52], which would complicate analysis.

The PRAs in Fig. 1 have comparable steric accessibility. The diameter of 5.8 Å shown for $Ru(NH_3)_6^{3+}$ ignores a second coordination sphere of eight water molecules at its octahedral faces, so we use its hydrated radius, as measured by Waysbort and Navon, of 3.9 ± 0.3Å [53], for both steric accessibility and the distance r from the nitroxyl oxygen surface at which it senses concentration upon collisional spin exchange (Eq. (4)). $Fe(CN)_6^{3-}$ is the smallest, with a steric radius of 3.1Å. Because of its negative shell/positive core structure, we take its distance r as zero during collisional spin exchange. NiEDDA^0 is hexadentate, similar to the charged PRAs with waters completing two ligand positions [54]. It lies between the charged PRAs in size.

PRA magnetic properties relevant to collisional spin exchange are spin quantum number S, effective magnetic moment μ, spin-lattice relaxation rate R_{1PRA}, and unpaired spin density in orbitals that overlap during a collision [49] (Table 4). Both $Ru(NH_3)_6^{3+}$ and $Fe(CN)_6^{3-}$ have $S = 1/2$, matching that of the unpaired nitroxide spin. They have spin-lattice relaxation rates of 400 and 10,000 GHz, respectively, and unpaired spin density of ~0.4% coupled to their outermost atoms [55–57]. Even though NiEDDA^0 has $S = 1$, we chose it as neutral because it has performed well in other accessibility studies [58] and because of its relaxation rate of 250 GHz [59].

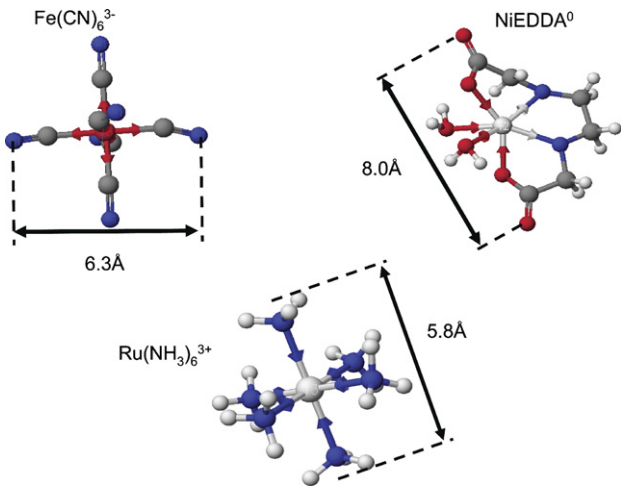

Fig. 1. Paramagnetic relaxation set chosen for the voltmeter set with modeled dimensions. Models are from Fujitsu Cache™.

Unlike these transition metal PRAs, unpaired spin density resides on the nitroxyl group alone [60] for a nitroxide and only the oxygen is sterically accessible, based on simple modeling. As a result only ~25% of the small nitroxide surface presents the spin density necessary for spin exchange.

Finally, our voltmeter PRAs are stable during experiments (easily past 20 h) with respect to ligand or central ion substitution as well as redox reactions [58,61–63] in aqueous buffer at pH 7 and 25 °C.

2.4. PRA calibration

Electrostatic potential measurements based on collisional spin exchange occur at atomic dimensions. If all the charge sources for the measured electrostatic potential reside within a Debye length of the nitroxyl oxygen surface then the ionic strength of the medium will not affect this potential. Calibrations made upon the highly localized electrostatic potentials of small nitroxides (Fig. 2) should indeed be possible and prove the high degree of accuracy achievable with appropriate PRAs. The PRA set (Fig. 1) was calibrated to determine the factors K_1^+ and K_1^- (Eq. (6)) in a series of experiments with small nitroxides in solution. Several uncharged nitroxides were measured first to determine first-order calibrations, and these were then refined by matching experimental values of V (Eq. (7)) for charged nitroxides TEMPO-choline (+1 charge) and carboxy-TEMPO (−1 charge) (Fig. 2) with those determined from Debye–Hückel theory.

The model distances shown in Fig. 2 are measured to the center of the nitroxyl oxygen. We define a nitroxyl oxygen reference surface as the patch over this oxygen through which all excited spin state transfers occur. The oxygen diameter of 1.5 and 1.0 Å for coordinated water are added to the model distance from the test charge to reach this surface in voltage calculations.

Our nitroxide test charges are approximately ellipsoids (Fig. 3A). For lower limit of the electrostatic potential, V_s, the nitroxide structure is ignored and the test charge is screened by point charge ions across the distance $d + r$, i.e. the distance d from test charge to nitroxyl oxygen sur-

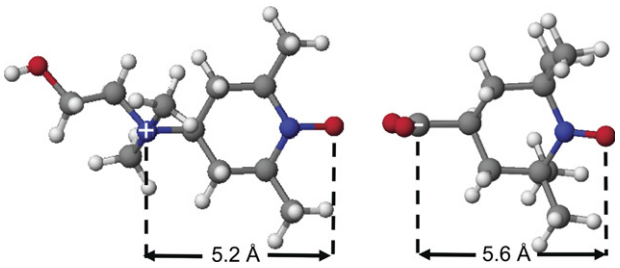

Fig. 2. Charged nitroxides used for PRA calibration. Left: positively charged TEMPO-choline. Right: negatively charged carboxy-TEMPO. Center-to-center distances from charged atoms to nitroxyl oxygen are shown.

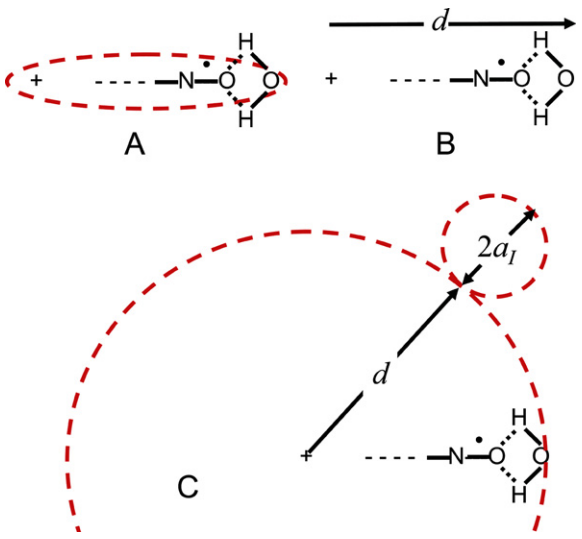

Fig. 3. Models for voltages produced by charged nitroxides.

face (Fig. 3B) plus distance r from this surface at which the charged PRA senses concentration:

$$V_s(d+r) = \frac{Q}{4\pi\varepsilon_0\varepsilon_r d}\exp\left(\frac{-(d+r)}{\lambda_D}\right) = \frac{184.6[\text{mV}\cdot\text{Å}]}{d+r}\exp\left(\frac{-(d+r)}{10\text{Å}}\right). \quad (8)$$

The Debye length λ_D is set to 10Å here using Eq. (9) (see Eq. 12.1–27 p.162 of [64]), based on the 90 mM ionic strength (μ) typical in our experiments.

$$\lambda_D = \left(\frac{\varepsilon_0\varepsilon_r k_b T}{2e^2 N_A \mu}\right)^{1/2} = \frac{3.04}{\sqrt{\mu[\text{mM}]}}[\text{Å}] \quad (9)$$

For a high limit of electrostatic potential, V_f, from each test charge finite ion sizes are assumed to calculate the "internal" electrostatic potential (Eq. 10 e.g., see p.327 in [65]), where $a = d + a_I$ and a_I are the steric radii of $Fe(CN)_6^{3-}$ and $Ru(NH_3)_6^{3+}$ (Fig. 3C).

$$V_f(r) = 184.6[\text{mV}\cdot\text{Å}]\left[\frac{1}{d+r} - \frac{1}{\lambda_D + a}\right] \quad (10)$$

Eq. (10) should reflect voltages measured with $Fe(CN)_6^{3-}$ more closely, because the intense electric field of its negatively charged shell partially saturates the water dielectric near its point of collision. $Ru(NH_3)_6^{3+}$ has a less intense electric field and measures several angstroms away from the oxygen surface, so values calculated with Eq. (8) should be closer to these measurements. Because these charged PRAs sense concentration at different r distances, they provide information about the gradient of the electrostatic potential near the nitroxide.

2.5. Separating R_1 and R_2 for small nitroxides

In the simplest analysis, nitroxide R_1 and R_2 increase linearly with added PRA [38].

$$R_1 \equiv R_{10} + \chi_1[\text{PRA}] \quad R_2 \equiv R_{20} + \chi_2[\text{PRA}] \quad (11)$$

We use these expressions to explain why lineheight saturation analysis is inadequate for our calibrations with small nitroxides. Some investigators have used $\chi_1 = \chi_2$ [38,43] as assumed in original spin exchange work with small nitroxides [49]. Since lineshape analysis provides R_1 values we do not make this assumption.

In the conventional EPR accessibility experiment on spin-labeled protein, lineheights Y are measured from derivative peaks of progressive saturation spectra and the resulting curve is fit to a semi-empirical equation [58,66,67]:

$$Y = \frac{A\sqrt{P}}{\left[1 + \frac{C^2P\gamma^2}{R_1R_2}\right]^{\varepsilon}}. \quad (12)$$

Here P is the power incident to the resonator, C is the cavity factor defined in Eq. (13) which converts this power to microwave magnetic field in the sample and $\gamma = 1.76\times10^7\ \text{s}^{-1}\,\text{G}^{-1}$.

$$H_1^2 \equiv C^2P \quad (13)$$

A, $P_{1/2}$ and ε are constants determined by fitting the lineheight curve. Constant ε ranges from 0.5 for completely inhomogeneous to 1.5 for completely homogeneous spectral lines [67,68]. Half saturation power $P_{1/2}$ is the power P at which the denominator in Eq. (12) equals 2.

$$P_{1/2} = \frac{(2^{1/\varepsilon}-1)R_1R_2}{C^2\gamma^2} \quad (14)$$

$P_{1/2}$ is proportional to R_1R_2, i.e.

$$(R_{10}+\chi_1[\text{PRA}])(R_{20}+\chi_2[\text{PRA}]) = R_{10}R_{20} + R_{10}\chi_2[\text{PRA}] + R_{20}\chi_1[\text{PRA}] + \chi_1\chi_2[\text{PRA}]^2. \quad (15)$$

For fast-tumbling small nitroxides, $R_1 \approx R_2$, making all terms important. This leads to a quadratic dependence of $P_{1/2}$ on PRA concentration, which we observe. At the other extreme, rigidly labeled proteins make the nitroxide tumble slowly in solution, so $R_1 \ll R_2$, p413 in [69]. Also, $\chi_{1,2}[\text{PRA}] \ll R_2$ for our PRAs, added from 0 to 10 mM. In this limit Eq. (15) is

$$(R_{10}+\chi_1[\text{PRA}])(R_{20}+\chi_2[\text{PRA}]) \cong R_{10}R_{20} + R_{20}\chi_1[\text{PRA}] \quad (16)$$

This differs slightly from the approximation presented in [38]. Here $P_{1/2}$ is proportional to R_1. Thus when experiments are performed to measure voltage at spin labels on proteins the change in $P_{1/2}$ is used in place of the change in R_1 (which replaces χ_1) in Eq. (7) with the same concentration of added charged and neutral PRA and under the assumption that ε and R_{20} remain constant. However, for very floppy spin labels on protein loops, this slow-tumbling approximation may be poor.

The quadratic dependence of $P_{1/2}$ for small nitroxides makes it impossible to determine changes in R_1 (χ_1) sepa-

rately for the general case of a partially homogeneous ($0.5 < \varepsilon < 1.5$) spectrum with lineheight fitting. Also, we wish to avoid approximating changes in R_1 as being proportional to changes in the square root of $P_{1/2}$, based the fast tumbling limit assumption that $R_1 = R_2$, because these calibrations are fundamental measurements that demand the least number of assumptions and the highest achievable accuracy. Therefore, we performed global lineshape analysis on progressive saturation spectra to directly separate R_1, R_2 and inhomogeneous linewidth Γ_G with PRA concentration across sets of saturation spectra for the central line ($I = 0$) of small ^{14}N nitroxides in this study. More et al. [70] pioneered global lineshape fitting of EPR spectra, applying it to estimate R_1 and R_2 changes for a spin-labeled porphyrin with and without high-spin Fe(III) chelated. They fitted the central line as we do, but used an inhomogeneous broadening function that included proton hyperfine splitting explicitly to the first order. More recently, Nielsen et al. [43] employed similar detailed global fitting for 8 spectral aspects of the central line of tempol to compare R_1 and R_2 measurements from CW progessive saturation and pulsed saturation recovery. Our focus is on the measurement of accurate relaxivity changes. So we are less concerned about accurate absolute relaxation rates and employ a simpler model for inhomogeneous broadening which has proven to be acceptable.

Nitroxide inhomogeneous broadening is caused by static local magnetic fields [71,72]. In small rapidly tumbling nitroxides, this broadening is dominated by the static dipolar interactions of the 12 methyl protons (superhyperfine splitting) [73]. We focus on the ^{14}N central line (I=0) and assume that inhomogeneous lineshape can be accounted for by a single Gaussian:

$$G(\Delta H) = \frac{1}{\sqrt{2\pi}\Gamma_G} \exp\left[-\frac{1}{2}\left(\frac{\Delta H}{\Gamma_G}\right)^2\right]. \tag{17}$$

In global lineshape fitting we convolve this inhomogeneous lineshape with the derivative Lorentzian lineshape, Eq. 4, p.589 in [74]:

$$L(\Delta H) \equiv \frac{A_{LL}\Delta H\sqrt{P}}{\left[1 + \left(\frac{\gamma\Delta H}{R_2}\right)^2 + \left(\frac{C^2 P \gamma^2}{R_1 R_2}\right)\right]^2}, \tag{18}$$

where A_{LL} is the lineshape constant, ΔH as the offset from resonant field center. Thus the lineshape $V(\Delta H)$ that is fit to the data is

$$V(\Delta H) = \int G(\Delta H')L'(\Delta H' - \Delta H)\mathrm{d}\Delta H'. \tag{19}$$

It should be clear that the experimental line acquired across a set of ten powers of progressive saturation, is fit by a single Gaussian line and a single Lorentzian line with global lineshape fitting.

Adding power P as a new dimension provides enough information to determine R_1, in addition to R_2, and Γ_G [73,75–81], thus achieving our primary goal of accurately determining relaxivities χ_1. Small nitroxides in deoxygenated solution exhibit discrete superhyperfine splitting. The effect of this partially resolved structure on fitting is reduced by setting nitroxide concentration at 0.5 mM [45] and by setting the field modulation amplitude close to the central linewidth in order to obtain the most accurate measurements of changes in R_1 and R_2 as PRA concentration is changed (relaxivities).

2.6. Experimental

Standard aqueous buffer for these experiments contained 20 mM Tris–HCl, 30 mM KCl, 5 mM $MgCl_2$, 0.1 mM EDTA, pH 7.5, 25 °C.

Sigma–Aldrich stocks. Tempone = 4-oxo-TEMPO, IASL = 4-(2-iodoacetimido)-TEMPO, MSL = 4-maleimido-2,2,6,6-tetramethyl-1-peridinyloxy, 4-Carboxy-TEMPO, IAPCPSL = 3-(3-(2-iodoacetimido)-propyl-carbamoyl)-proxyl, *N*-Acetyl-L-cysteine methyl ester, $Cr(C_2O_4)_3^{3-}$ from potassium chromium (III) oxalate trihydrate, $Co(CN)_6^{3-}$ from potassium hexacyanocobaltate(III), $Fe(CN)_6^{3-}$ from potassium hexacyanoferrate(III), $Co(NH_3)_6^{3+}$ from hexamine cobalt(III) chloride, $Ru(NH_3)_6^{3+}$ from hexaammine ruthenium(III) chloride.

Other stocks. Perdeuterated tempone = 4-Oxo-2,2,6,6-tetramethylpiperidine-d16-1-oxyl from C/D/N Isotopes, TEMPO-choline = 4-(*N*,*N*-dimethyl-*N*-(2-hydroxyethyl)) ammonium-2,2,6,6-tetramethylpiperidine-1-oxyl chloride from Invitrogen, *N*-acetyl-L-cysteine allyl ester from Toronto Research Chemicals, PEG derivatized resin beads are Novabiochem 01-64-0100 PEGA amino resin, NiEDDA^0 was from a stock prepared by Tara Kirby as described previously [67].

Labeling. ASL-cys-methyl and ASL-cys-allyl cases were formed by adding fresh cysteine stocks at 0.2 M in DMF to equimolar amounts of 0.2 M IASL DMF stocks, diluting these mixtures to 1mM with standard buffer shifted to pH 9 with KOH for labeling at 25 °C for 4 h and then on ice for 20 h to ensure complete labeling. At the end of labeling pH was returned to 7.5 with HCl. PEG beads have $\sim 2 \times 10^{14}$ PEG chains per cross-linked resin bead with an amine on the distal end of each chain. These were swelled in MeOH to ~3 mM and labeled by adding 0.2 M MSL in DMF at high concentration. The beads were then washed in MeOH and packed over glass wool in a segment of 22 gauge thin-wall teflon to form a 22 mm long column over which buffer solutions with different PRA concentrations were washed for experiments achieving ~1 label per bead as judged by spin counting. ASL-S1 was rabbit myosin S1 obtained by chymotryptic digestion and aliquots labeled with the procedure in [82], with stocks stored for use in LN_2 with 20% added glycerol. Aliquots of ASL-S1 were cleaned and concentrated with 0.5 ml 50 kD MWCO PES Millipore Ultrafree spin concentrators on the day of the experiment to put EPR sample concentration at 0.36 mM after mixing with PRA stocks.

Sample handling. To keep relaxivity contrast high between PRAs, small nitroxide concentration was set to

0.5 mM, and each sample was deoxygenated for at least 10 min in nitrogen gas at ~2 atmospheres pressure (flow rate 100 L/h) before recording spectra. This gas flow was also used to control temperature at 25.0 °C during acquisition, limiting temperature rise to 0.040 °C/mW of incident power, as calibrated by the EPR-detected shift in the phase transition of DMPC vesicles [83]. Spectra were acquired with a Bruker E500 spectrometer using a 4122shq cavity with quartz cavity dewar insert. Aqueous sample length was limited to 13 ± 1 mm in a ~45 mm segment of 22 gauge thin-wall Teflon, critosealed on each end. This length limits the increase in $P_{1/2}$ due to nonuniform saturation to less than 15% based on a squared cosine function model of the resonator standing wave. Sample depth is set to ±0.1 mm accuracy by impaling one end of the teflon segment on 22 gauge wire, friction fit in a custom depth gauge that clips atop the cavity dewar. This segment is aligned within the quartz dewar by an insert made from 100 μL wiretrol capillary with nested P200 pipette tips on each end cut to fit and parafilmed at the top, to force all cooling gas over the segment containing the sample.

Calibration. A cavity factor C (Eq. (13)) of 1.91 G/W$^{1/2}$ was determined by PADS calibration with modulation amplitude set at 1/4 of the peak-to-peak linewidth [84]. The sensitivity of relaxivity to modulation amplitude was tested by varying CrOx concentration from 0 to 10 mM against 0.5 mM tempone, finding that relaxivities χ_1 and χ_2 were independent of modulation amplitude over the range from 0.1 and 0.5 G.

Spectral acquisition. Progressive saturation spectra of each ^{14}N nitroxide derivative central line were acquired at 10 values for P from 0.6 to 40 mW (0.076–0.606 Gauss H_1) for several concentrations of each PRA with modulation amplitude set to approximately half the low-power linewidth. Global lineshape fitting to Eq. (19), to determine both R_1 and R_2 for rapidly tumbling nitroxides, was performed using a program designed in Visual Basic by Igor V. Negrashov. Simple lineheight fitting to Eq. (14), which is sufficient only for slowly tumbling nitroxides, was done in the standard way [67,85].

3. Results

Measured small nitroxide relaxivities χ_1 (and χ_2), as defined in Eq. (11) for each PRA, are the central findings of this investigation (Table 2). These come from the observed linear dependence of nitroxide R_1 and R_2 on PRA concentration between 0 and 10 mM, as illustrated in Figs. 6–10. Some nonlinearity is observed in a few R_2 cases at low [PRA]. We assume that this is due to "short circuiting" of the coupling between hyperfine lines due to nitroxide-nitroxide collisions by the added PRA. At the other end of the PRA concentration range, tempone with added $Fe(CN)_6^{3-}$ and MSL-PEG with added $Fe(CN)_6^{3-}$ are the only cases where divergence from linearity occurs at ~8 mM and above (Fig. 9). In particular, the relaxation rates become extremely large for tempone with added $Fe(CN)_6^{3-}$ above 10 mM, suggesting coordination forces that are strong enough between these two smallest agents to form a complex. This may be similar to the evidence for a hydrophobic interaction between oxygen and small nitroxides found by Diakova and Bryant [86]. Nevertheless, in all cases there is an extensive linear range over which relaxivities can be measured (Table 2). In all small nitroxide cases, χ_2 is larger (by 10–70%) than χ_1.

Measured χ_1 for NiEDDA^0 is essentially constant across the small nitroxide experiments, supporting the assumption that it is neutral. Tempone and IAPCPSL values are the furthest from the rest, being about 10% higher. IAPCPSL is the only proxyl small nitroxide tested. A few $Cr(C_2O_4)_3^{3-}$ (CrOx) experiments are reported (Table 2) because it is often used in EPR accessibility studies. CrOx small nitroxide χ values are indeed 2–3 times larger than corresponding values of $Fe(CN)_6^{3-}$ [87]. We avoided CrOx because of its slower relaxation rate (Table 4), but primarily because with hydration, its diameter would be a few angstroms larger than our other PRAs. The abnormally low ASL-S1 χ_1 results for CrOx confirm this.

3.1. Correction factors and voltages

To find the most neutral nitroxide case the ratios of charged-to-neutral PRA relaxivity in Table 3 are used in expression $|\ln(\chi_1^-/\chi_1^+)|$ to find a minimum. The minimum occurs because charged PRA concentrations shift in opposite senses when a voltage is present. The IASL-labeled cysteine cases (ASL-cys-allyl/methyl) come closest to having the nitroxyl oxygen at neutral potential, providing initial K factors (Eq. (6)) of 1.70 for $Fe(CN)_6^{3-}$ and 1.50 for $Ru(NH_3)_6^{3+}$. Applying these to TEMPO-choline and carboxy-TEMPO (Fig. 2), $Fe(CN)_6^{3-}$ measured voltages are +12.3 mV and −14.8 mV, respectively, while $Ru(NH_3)_6^{3+}$ voltages are +4.7 mV and −4.7 mV. The $Fe(CN)_{63-}$ values match finite ion model (Eq. (10)) voltages in Table 1 within 3 mV. By adding an offset of +1.9 mV, both are just 6% lower than calculated. Similarly, the $Ru(NH_3)_6^{3+}$ voltages agree with the point charge model (Eq. (8)) shown in Table 1 to 0.2 mV. We refine the K^+ factor to add +0.2 mV offset. The refined K factors are then 1.35 for $Fe(CN)_6^{3-}$ and 1.54 for $Ru(NH_3)_6^{3+}$. These are used to determine measured voltages in the last column of Table 3 and future measurements using Eq. (7).

Because measured results, determined from Eq. (7), match those from simple Debye–Hückel theory so closely, they support the model that charged PRAs are completely

Table 1
Model voltages in [mV] at the nitroxyl oxygen surface for the two charged PRAs

Test nitroxide	$Fe(CN)_6^{3-}$		$Ru(NH_3)_6^{3+}$	
	Eq. (8)	Eq. (10)	Eq. (8)	Eq. (10)
TEMPO-choline	11.1	15.1	5.0	7.4
Carboxy-TEMPO	−9.9	−13.7	−4.5	−6.9

dissociated from counterions when they collide at the nitroxyl oxygen reference surface. In most cases $Fe(CN)_6^{3-}$ voltages are significantly larger than $Ru(NH_3)_6^{3+}$ voltages. This fits our simple model that it measures concentration at $r = 0$ distance from the oxygen surface while $Ru(NH_3)_6^{3+}$ measures concentration at $r = 4$ Å. Using IAPCPSL and deuterated tempone results, we estimate the correction factor for CrOx, $K^{CrOx} = 2.4$ and use this to present voltages measured with this PRA in Table 3.

Even small nitroxides selected to be ionically neutral display small voltages at their nitroxyl oxygen, probably due to dipoles from coordinated water. Most notable is IASL at 5 mV, an ionically neutral six membered ring nitroxide which should present the positive pole of an electrostatic dipole at its nitroxyl oxygen in response to strongly electronegative Iodine. IAPCPSL is the lone proxyl showing slightly negative voltage whereas the remaining neutrals show slightly positive voltages. The MSL-PEG column case has one MSL nitroxide label reacted out of a sea of 2×10^{14} amines that reside at the distal ends of PEG chains attached to each resin bead, which explains why $Ru(NH_3)_6^{3+}$ and $Fe(CN)_6^{3-}$ both measure a +5 mV potential.

Considering all the calculated voltages an overall accuracy of 1 mV is evident for our voltmeter PRAs against small nitroxides.

3.2. Comparing ASL-S1 voltages from lineshape and lineheight fitting

Rabbit myosin S1 labeled at Cys707 (SH1) with no nucleotide present (ASL-S1) has turned out to be a good choice to validate our PRAs for three reasons. First, the label resides in a tight crevice such that its spectrum indicates strong immobilization. So the site tests our PRAs at the low-accessibility limit [88] and provides an extreme test of global lineshape fitting, as Fig. 12 and Table 2 indicate. The $Fe(CN)_6^{3-}$ R_1 and R_2 results from lineshape fitting are clearly linear functions of PRA concentration while the remaining PRAs show more scatter in Fig. 12. Second, the pK of the SH1 thiol is known to be 6.28 [15] which explains the high reactivity that favors its specific labeling. Third, this region of S1 is relatively thin so there is water above and below the site, which allows the potential causing the thiol pK shift to be estimated at the nitroxyl oxygen surface using Eq. (10).

Voltages for ASL-S1 in the apo state at the spin label are +3 and +1 mV for $Fe(CN)_6^{3-}$ and $Ru(NH_3)_6^{3+}$ from lineshape fitting (Table 3). These voltages are +4 and +3 mV, respectively, using more accurate lineheight fitting based on PRA concentrations set to 5 mM.

Taking the in situ pK of a cysteine thiol in an electrostatically neutral region to be 8.55 ± 0.03 [14], the voltage responsible for the pK shift to 6.28 at SH1 is $V_s = 135$ mV, based on the Tanford–Roxby equation [89] at 25 °C:

Table 2
PRA relaxivities from nitroxide experiments

Experiment	PRA	χ_1 [MHz/mM]	χ_2 [MHz/mM]	$\frac{\chi_2}{\chi_1}$
Tempone	Cr	1.9 ± .1	2.94 ± .05	1.5
Tempone	Fe	0.72 ± .02	0.91 ± .03	1.3
	Ni	0.67 ± .02	0.95 ± .01	1.4
	Ru	0.92 ± .02	1.28 ± .02	1.4
IASL	Fe	1.62 ± .02	2.06 ± .03	1.3
	Ni*	0.61 ± .01	0.77 ± .01	1.3
	Ru	0.81 ± .02	1.01 ± .05	1.2
IAPCPSL	Cr	1.36 ± .06	2.30 ± .04	1.7
	Fe	0.71 ± .01	0.86 ± .02	1.2
	Ni*	0.68 ± .01	0.89 ± .02	1.3
	Ru	1.14 ± .03	1.42 ± .05	1.2
ASL-cys-allyl	Fe	1.01 ± .07	1.58 ± .03	1.6
	Ni*	0.58 ± .01	0.93 ± .01	1.6
	Ru	0.91 ± .01	1.36 ± .01	1.5
ASL-cys-methyl	Fe	1.04 ± .01	1.60 ± .03	1.5
	Ni	0.61 ± .01	0.91 ± .01	1.5
	Ru	0.90 ± .01	1.35 ± .02	1.5
Deuterated tempone	Cr	1.76 ± .02	2.84 ± .01	1.6
	Fe	1.17 ± .04	1.34 ± .03	1.1
	Ni	0.65 ± .01	0.90 ± .01	1.4
	Ru	0.91 ± .04	1.17 ± .02	1.3
TEMPO choline (+)	Fe	4.7 ± .1	6.5 ± .1	1.4
	Ni	0.62 ± .01	1.02 ± .01	1.6
	Ru	0.54 ± .01	1.06 ± .01	2.0
Carboxy TEMPO (−)	Fe	0.180 ± .005	0.22 ± .01	1.2
	Ni	0.60 ± .02	0.94 ± .02	1.6
	Ru	1.56 ± .06	2.17 ± .02	1.4
MSL-PEG bead column	Fe	1.4 ± .2	0.45 ± .02	0.32
	Ni	0.58 ± .01	0.42 ± .03	0.72
	Ru	0.528 ± .005	0.54 ± .01	1.0
ASL-S1 Myosin S1 Labeled at Cys707	Cr	0.040 ± .002		
	Fe	0.069 ± .001		
	Ni*	0.044 ± .001		
	Ru	0.052 ± .004		

Cr = $Cr(C_2O_4)_3^{3-}$, Fe=$Fe(CN)_6^{3-}$, Ni=NiEDDA^0 and Ru = $Ru(NH_3)_6^{3+}$.
* Indicates NiEDDA^0 solutions with $Co(NH_3)_6^{3+}$ and $Co(CN)_6^{3-}$ diamagnetics in solution.

$$V_S = 59.1 \text{ mV}[pK(\text{insitu}) - pK(\text{observed})]. \quad (20)$$

This 135 mV potential results from essentially one positive charge. Molecular modeling indicates that the distance from the cysteine thiol to the nitroxyl oxygen for a spin label reacted at Cys707 is 9.0 Å. Using Eq. (10) we calculate that the potential measured by $Fe(CN)_6^{3-}$ should be +6 mV (observed +4 mV) and by $Ru(NH_3)_6^{3+}$ +4 mV (observed +3 mV). So even in this extreme case measurements are accurate to within a few mV.

3.3. Measured R_{10} and R_{20}

All small nitroxide R_{10} relaxation rates are around 1 MHz as expected. In this fast-tumbling limit R_{20}/R_{10} ranges from 1.4 to 3.3 in our global lineshape fitting results.

Table 3
Charged-to-neutral PRA (NiEDDA^0) R_1 relaxivity ratios and corresponding voltages indexed by charged PRAs indexed as in Table 2

Experiment	±PRA	$\frac{\chi_1^{\pm}}{\chi_1^0}$	$\lvert \ln \frac{\chi_1^-}{\chi_1^+} \rvert$	V [mV]
Tempone	Cr	2.85		+1.5
Tempone	Fe	1.08	0.24	(−1.9)
	Ru	1.37		+1.0
IASL	Fe	2.58	0.63	+5.5
	Ru	1.37		+1.0
IAPCPSL	Cr	2.11		−1.0
	Fe	1.04	0.47	−2.2
	Ru	1.67		−0.7
ASL-cys-allyl	Fe	1.70	0.09	+2.0
	Ru	1.55		+0
ASL-cys-methyl	Fe	1.70	0.15	+2.0
	Ru	1.46		+0.5
deuterated tempone	Cr	2.70		+1.1
	Fe	1.79	0.24	+2.4
	Ru	1.41		+0.7
TEMPO choline (+1)	Fe	7.12	2.1	+14.2
	Ru	0.87		+4.9
Carboxy TEMPO (−1)	Fe	0.30	2.1	−12.9
	Ru	2.6		−4.5
MSL-PEG column	Fe	2.4	0.38	+4.9
	Ru	0.91		+4.5
ASL-S1	Cr	1.1		(−6.6)
	Fe	2.0	0.36	3.4
	Ru	1.4		0.8

Voltages distorted by short ranges forces, as specified in the text, are given in parentheses.

As expected, this ratio increases to 100 for the rigid spectrum of IASL reacted at cys707 on myosin S1 in the apo state (ASL-S1). The mobile spectrum of MSL tethered to a bead with a polyethylene glycol segment (MSL-PEG) has a ratio of 3 and provides a lower limit for the mobile spectra from labels on protein loops. This low ratio suggests that lineshape may be more appropriate than lineheight fitting to determine voltages from mobile spectra with conventional EPR.

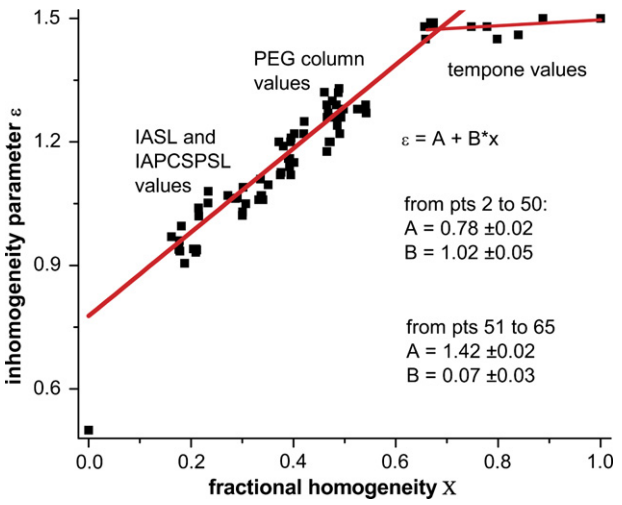

Fig. 4. Scatter plot of inhomogeneity parameter from lineheight versus fractional homogeneity from lineshape fitting.

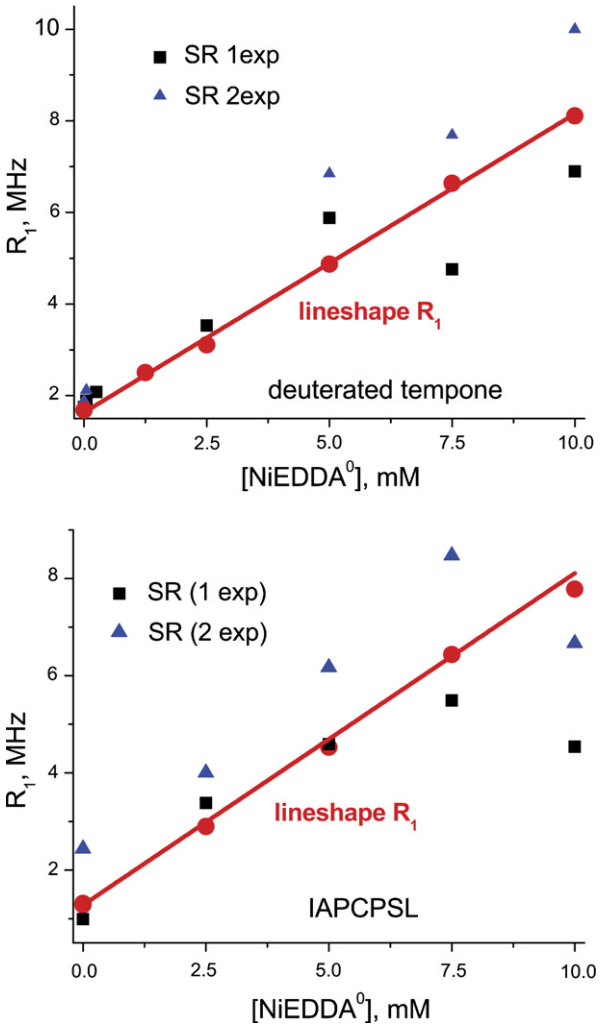

Fig. 5. R_1 measured from saturation recovery decays using 1 (squares) and 2 (triangles) exponential fits compared with R_1 from lineshape fitting (circles) for deuterated tempone and IAPCPSL with NiEDDA^0 added from 0 to 10 mM.

Table 4
Aqueous PRA magnetic properties at 25 °C

paramagnet	Spin S	T_{PRA} (ns)	μ_{eff} (μ_B)
$Cr(C_2O_4)_3^{3-}$	1.5	0.5 (a)	3.44 (f)
$Fe(CN)_6^{3-}$	0.5	0.0001 (b)	2.33 (g)
NiEDDA^0	1	0.0043 (c)	3.21 (h)
$Ru(NH_3)_6^{3+}$	0.5	0.0025 (d)	2.15 (i)
O_2	1	0.0075 (e)	1.2 (j)
Nitroxide	0.5	~1000	1.73

T_{PRA} is PRA spin-lattice relaxation time and μ_{eff} is PRA magnetic moment in Bohr magnetons. (a) Table 8, p.105 in [93]; (b) by NMRD [94]; (c) hexaqua Ni complex [59]; (d) by NMR [55] (e) by NMR [95]; (f) [96]; (g) p.935 [61]; (h) [54]; (i) [97]; (j) [98].

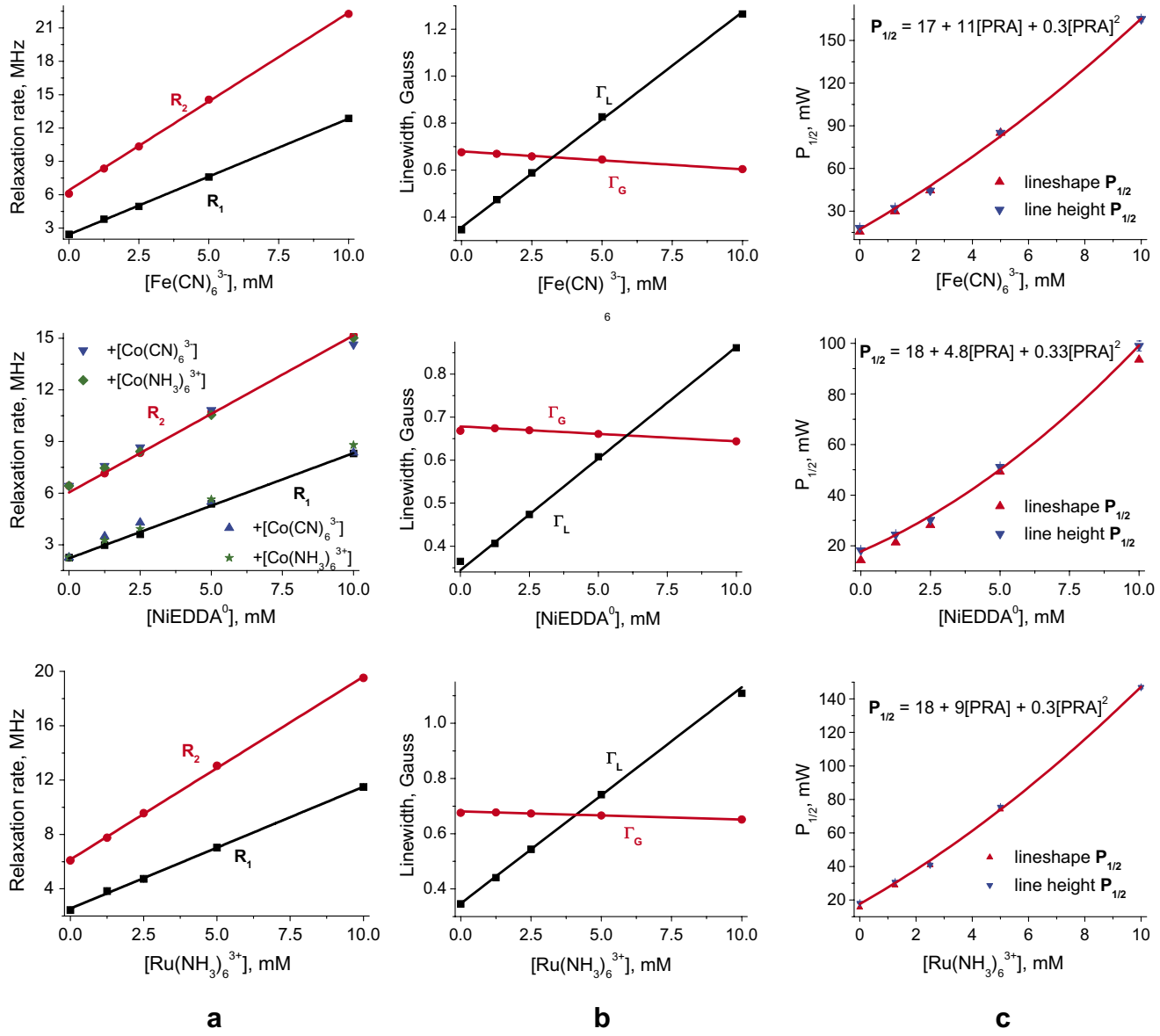

Fig. 6. Effects of PRAs on the saturation of ASL-cys-methyl. Values plotted in columns (a) and (b) come from global lineshape fitting based on the convolution of Eq. (18) with Eq. (17) show linear increases in R_1 and R_2 and a decrease in Γ_G with added PRA in each case. Downward pointing triangles in column (c) are half saturation values determined directly from lineheight fitting using Eq. (12). For this, as in other small nitroxide cases, curves usually have quadratic curvatures. Upward pointing triangles are half-saturation values generated from the combination of lineshape R_1, R_2 and ε using. Fig. 4 and Eq. (14). These are matched to lineheight values at 5 mM with constants from 1.0 to 1.4 across all data sets, here 1.24 for all PRA cases. The close fit between curvatures validates the accuracy of relaxivities as determined from lineshape fitting and this is found in all experiments. The constants indicate error in the absolute values of R_1, R_2 and ε. Spectra with NiEDDA^0 were taken with the specified diamagnetic ions to balance ionic strength with the charged PRA cases. As shown explicitly in the NiEDDA^0 case of column (a), these additions did not change the measured parameters.

3.4. Scatter plot between inhomogeneity parameter and fractional homogeneity

Haas et al. estimated the effects of inhomogeneous broadening on lineheight fitting with simulated spectra [90]. Our goal is simpler here in that we wish to show consistency between lineshape and lineheight results by discerning the functional relationship of inhomogeneous and homogeneous aspects of small nitroxide spectra. We assume that this relationship is valid for all nitroxide spectra. In Figs. 6–12, half-saturation power $P_{1/2}$ curves from lineheight fitting are compared to $P_{1/2}$ curves based on Eq. (14) using R_1 and R_2 derived from global lineshape fitting. To set the inhomogeneity parameter ε, we determine its relationship with the ratio of $\Gamma_L = R_2/\gamma$ to total linewidth across the data set, which we term the fractional homogeneity X. Experimental values of fractional homogeneity are determined by combining $\Gamma_L = R_2/\gamma$ and Γ_G in the linewidth relation found by Dobryakov and Lebedev to recapitulate the total peak-to-peak linewidth Γ_{pp} without saturation broadening [91] in Eq. (21). These values (not shown) are just below all experimental linewidths. We

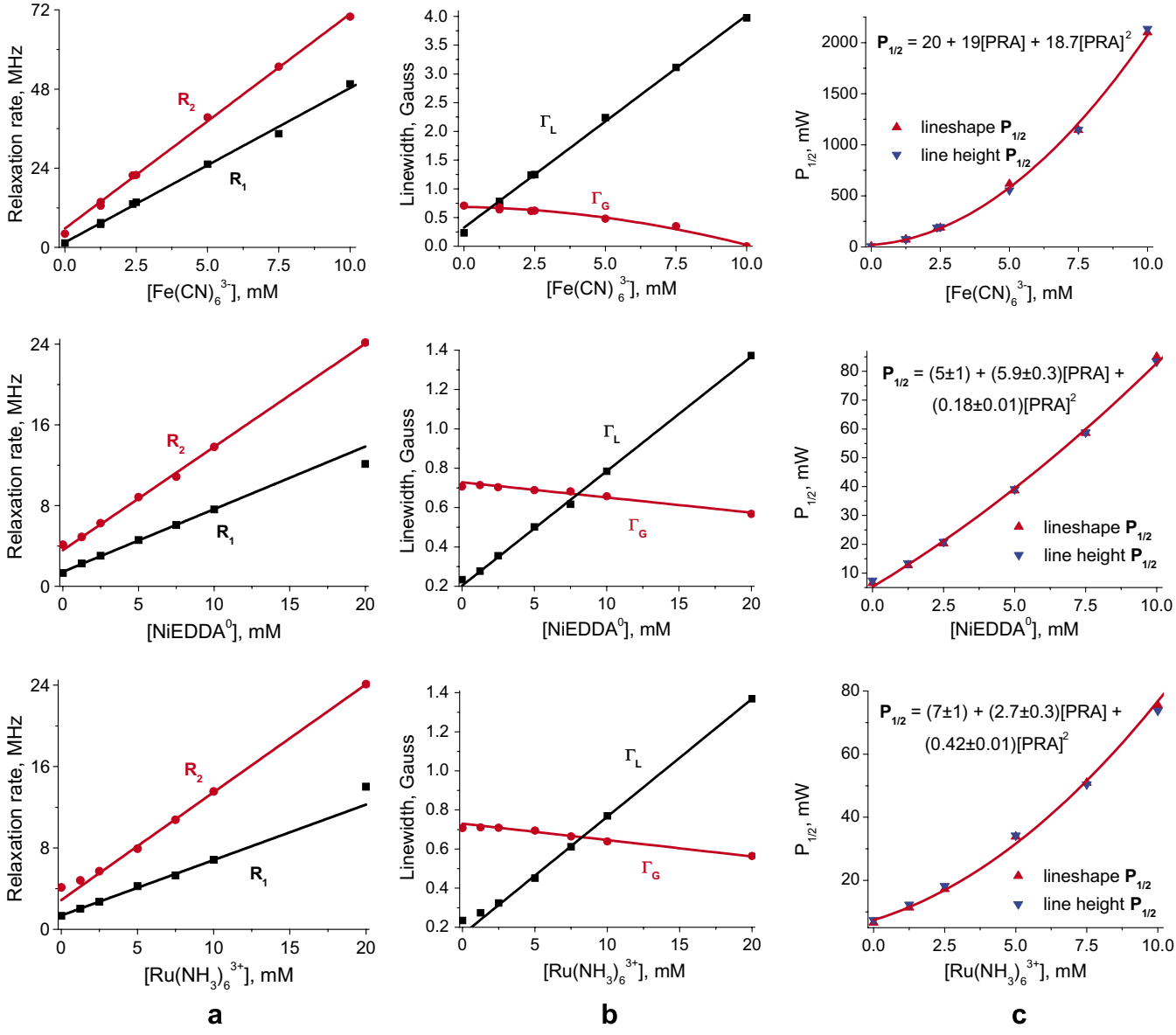

Fig. 7. Positively charged TEMPO-choline. Values plotted as in Fig. 6. Positive voltage at the nitroxyl oxygen enhances the interaction with $Fe(CN)_6^{3-}$ based on the much larger relaxation rates in column (a). The loss in inhomogeneous broadening in column (b) is also much greater and the quadratic curvature of half-saturation power $P_{1/2}$ is column (c) is much more pronounced. The weaker interaction of $Ru(NH_3)_6^{3+}$ is associated with more divergence from linearity near zero PRA concentration for both linewidths. The half-saturation power curves from line height (downward triangles) match lineshape results when the latter are multiplied by 1.16, 1.27 and 1.29 in column (c) for added $Fe(CN)_6^{3-}$, $NiEDDA^0$ and $Ru(NH_3)_6^{3+}$, respectively.

define the ratio of the Lorentzian component to this total linewidth as the fractional homogeneity in Eq. (22).

$$\Gamma_{pp} = \frac{\Gamma_L}{\sqrt{3}} + \sqrt{\frac{\Gamma_L^2}{3} + 4\Gamma_G^2} \tag{21}$$

$$X \equiv \frac{2\Gamma_L}{\sqrt{3}\Gamma_{pp}} \tag{22}$$

The scatter plot in Fig. 4 combines fractional homogeneity from lineshape analysis with the inhomogeneity parameter ε determined from lineheight fits using the same set of progressive saturation spectra, selecting cases with lineheight peaks below 40 mW and ε values that increase or remain the same as PRA concentration increases. The resulting scatter plot fits provides ε values to generate $P_{1/2}$ curves from lineshape R_1 and R_2 using Eq. (14). $P_{1/2}$ curves match well in all cases within a constant, column C of Figs. 6–12 provide specific examples.

3.5. Absence of dipolar broadening checked

A control experiment was performed to verify that total dipolar broadening was low for our fast-relaxing PRAs. The increase in half-saturation power, $\Delta P_{1/2}$, due to

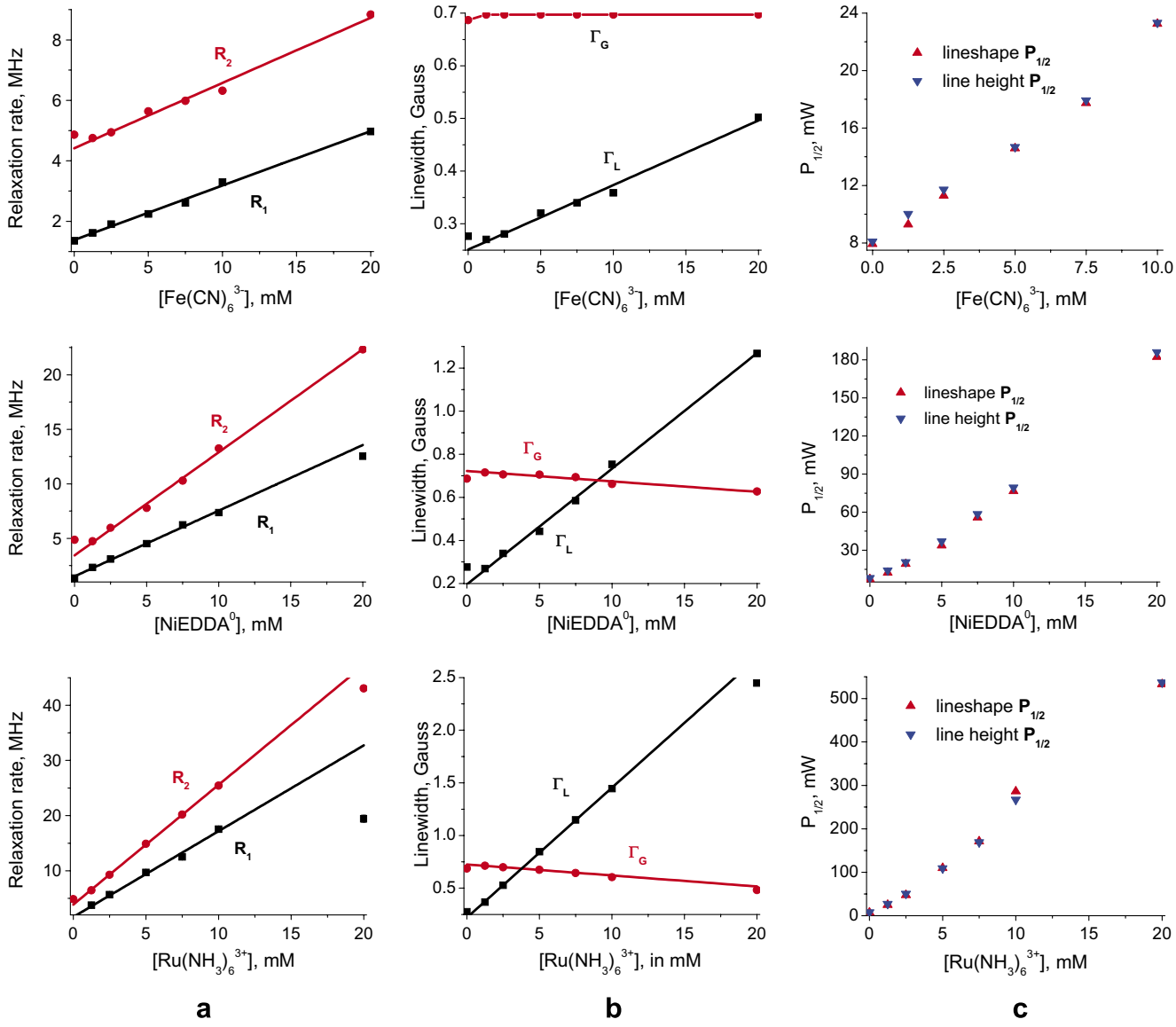

Fig. 8. Negatively charged carboxy TEMPO. Values plotted as in Fig. 6. Here the spin exchange interaction is reversed from Fig. 7 with the $Ru(NH_3)_6^{3+}$ interaction enhanced. Lineshape half-saturation powers plotted as upward triangles are multiplied of 1.33, 1.21 and 1.21 in column (c) for added $Fe(CN)_6^{3-}$, $NiEDDA^0$ and $Ru(NH_3)_6^{3+}$, respectively, to match corresponding values from line height saturation, similar to Fig. 7.

5 mM $Fe(CN)_6^{3-}$ against IASL-labeled myosin S1 at 25 °C changed from 33.7 mW at 1 cP viscosity to 3.32 mW at 10 cP. The 10 cP case was created by adding 60% glycerol by weight in solution.

3.6. Lineshape vs saturation recovery R_1 values

R_1 data from lineshape fitting agrees with that from saturation recovery for deuterated tempone and IAPCPSL with $NiEDDA^0$ added from 0 to 10 mM (Fig. 5).

Pulsed saturation recovery measurements were made at the National Biological EPR Center in Milwaukee. They were performed with a 300 nS excitation pulse at microwave field amplitude from 1.0 to 2.0 G and a low power microwave observing field of ~50 μG. Decays were acquired for 2 μS.

4. Discussion

4.1. Dipolar broadening error limits for PRAs

Nitroxide relaxation can occur through both collisional spin exchange and magnetic dipolar interactions. Dipolar interactions come in the form of static field heterogeneity (increasing linewidth) and resonant relaxation (assumed to increase R_1 and R_2 equally) and are often assumed to be insignificant for paramagnetic ions in solution [92], but some effects have been reported [46]. By selecting fast-relaxing PRAs here, we ensure that collisional spin exchange is strongly favored over dipolar interactions. Since X-band EPR involves resonant absorption at 10^{10} Hz, PRAs that relax at significantly faster rates should have no significant overlap in spectral density or static

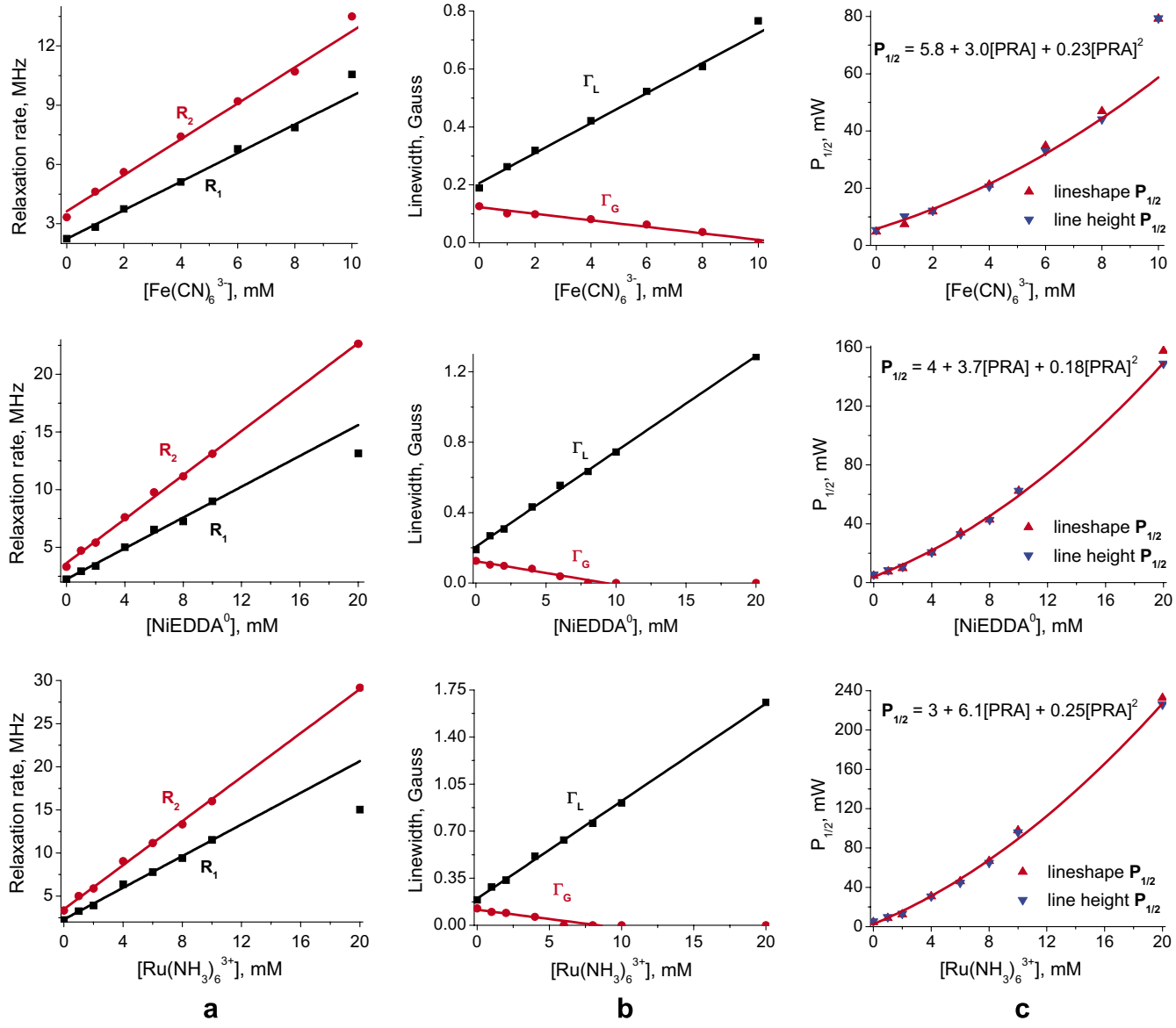

Fig. 9. Tempone spin relaxation results. Values plotted as in Fig. 6. Tempone is the smallest nitroxide tested. R_1 and R_2 go strongly supra-linear for $Fe(CN)_6^{3-}$ past 9 mM in column (a). This case is notable as the pairing of the smallest nitroxide with the smallest PRA. Inhomogeneous broadening is also minimal, going to zero between 7 and 10 mM of added PRA in column (b). Half saturation power plots in column (c) match when all lineshape-derived values are multiplied by 1.0, reflecting near-homogeneity.

broadening and so produce no observable dipolar broadening. We wish to estimate the broadening for each of our PRAs. To do so, we extrapolate experiments between 0.5 mM tempone and the paramagnetic complex $Cu(en)_2(H_2O)_2^{2+}$ done by Anisimov [59]. Table 3.3 on p.133 of [49] recapitulates this work with corrections.

In those experiments glycerol-water mixtures were used at 25 °C to decrease translational diffusion and so minimize spin exchange. The residual tempone linewidth due to the combination of static dipolar broadening and broadening from dipolar relaxation was limited to 12% of that found in water with $Cu(en)_2(H_2O)_2^{2+}$ added from 0 to 50 mM, i.e. $\Gamma_D/\Gamma_{SE} < 0.12$. We extrapolate from this limit to calculate corresponding limits for our PRAs using the relevant dipolar term from theory of proton relaxation enhancement with dissolved paramagnetic ions formulated by Bloembergen and Morgan [99,100], repeated in Eq. (23).

$$\Gamma_D \propto \frac{\mu_{eff} T_{PRA}}{15}\left(7 + \frac{13}{1 + (\omega_s T_{PRA})^2}\right) \tag{23}$$

We normalize for linewidth using 1.47 G for 10 mM $Cu(en)_2H_2O_2^{2+}$ with 0.5mM tempone in water, p.133 in [49] and use measured linewidths of 10 mM $[Cr(C_2O_4)_3^{3-}$, $Fe(CN)_6^{3-}$, NiEDDA^0, $Ru(NH_3)_6^{3+}]$ from our 0.5 mM tempone experiment = [1.64, 0.53, 0.55, 0.72] G. Then $Cu(en)_2H_2O_2^{2+}$ values $\mu_{eff} = 1.9$ [61] and $T_{PRA} = 2.7 \times 10^{-9}$ s [59] are combined with values from Table 4 to

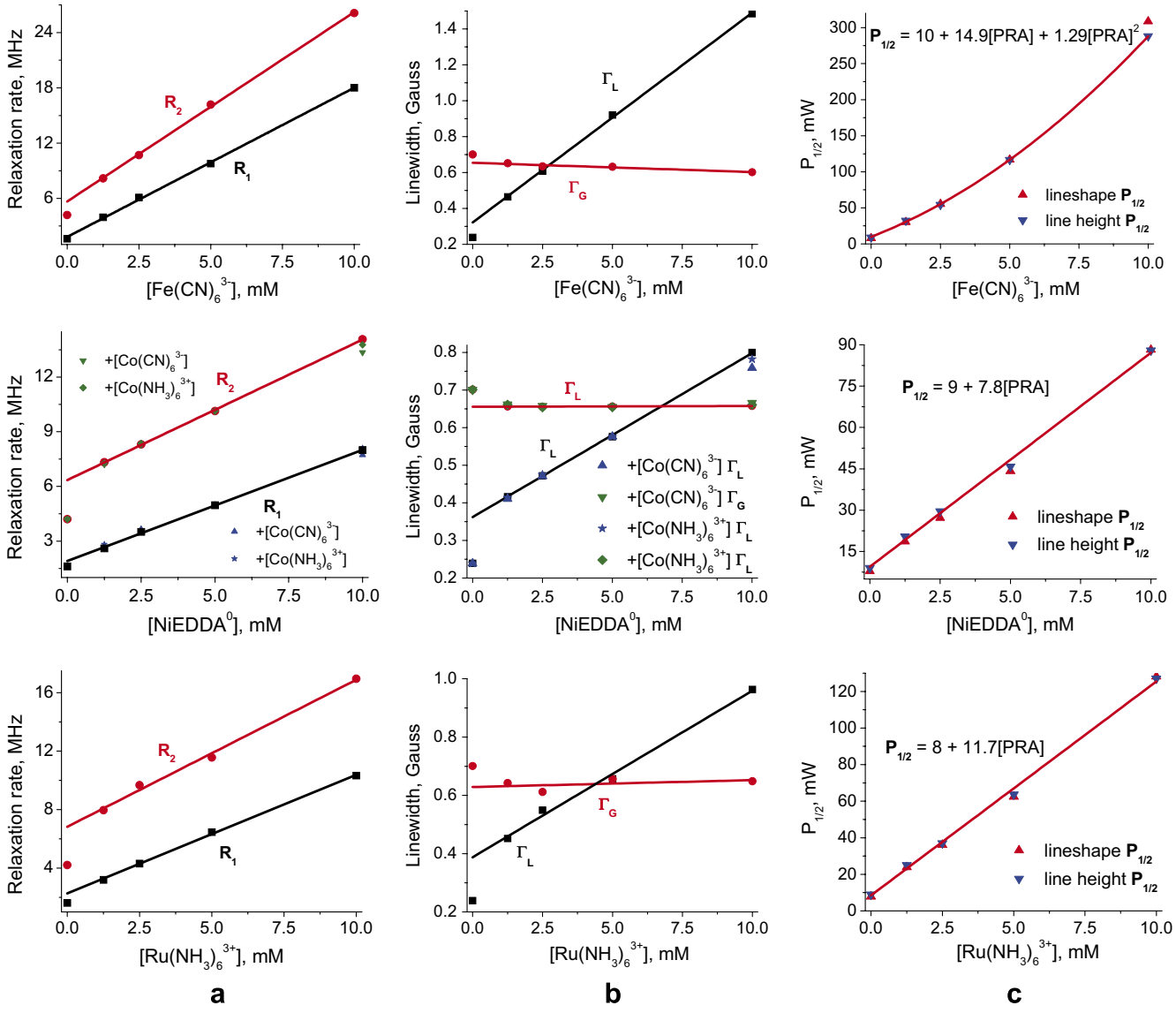

Fig. 10. Results for IASL. Values plotted as in Fig. 6. Small nitroxide IASL is unique because it exhibits a comparatively large initial collapse in inhomogeneous linewidth Γ_G between 0 and 1.25 mM added PRA, correlating with a nonlinear upward shift in $R_2(\Gamma_L)$ as seen in columns (a) and (b). This and the fact that superhyperfine splitting is prominent suggests two proton populations, one easily relaxed and the other largely unaffected by added PRA Note that more weakly interacting PRAs NiEDDA^0 and $Ru(NH_3)_6^{3+}$ show the largest nonlinearity in columns (a) and (b) and essentially linear $P_{1/2}$ curves in column (c). For NiEDDA^0 diamagnetic ions were added at the same concentration to balance ionic strength, which did not change the results, as indicated in columns (a) and (b).

form ratios based on Eq. (23) ($\omega_s = 5.9 \times 10^{10}$ rad/s) for upper bounds on broadening due to dipolar relaxation as $[Cr(C_2O_4)_3^{3-}$, $Fe(CN)_6^{3-}$, NiEDDA^0, $Ru(NH_3)_6^{3+}] =$ [32,0.0015, 0.15, 0.04]%.

4.2. Effective spin exchange rates compared to diffusion-controlled model

The spin exchange rate constants for NiEDDA^0, $Fe(CN)_6^{3-}$, $Ru(NH_3)_6^{3+}$ and $Cr(C_2O_4)_3^{3-}$ are 0.60, 0.81, 0.92 and 1.4 MHz/mM, respectively, against small six-membered ring nitroxides in aqueous buffer at 25°C. These come from measured increases in R_1 (χ_1) and so represent complete transfers of the excited spin state, much lower than the 3.6 MHz/mM rate anticipated for aqueous diffusion controlled reactions, p.154 in [49]. These values are reasonable considering other k_e measurements for transition metal complexes against nitroxides as given on p7 in [49]. We determine the probability of spin exchange for $Fe(CN)_6^{3-}$ collisions with nitroxides is $0.81/3.6 = 0.22$, matching the value of 0.2 found by [50].

4.3. Application ranges for lineheight and global lineshape fitting

In future voltage measurements approximate forms of Eq. (7) will be used based on ratios of parameters between charged and neutral PRAs. In the fast tumbling limit $R_1 = R_2$ proves adequate, allowing the ratio to be between

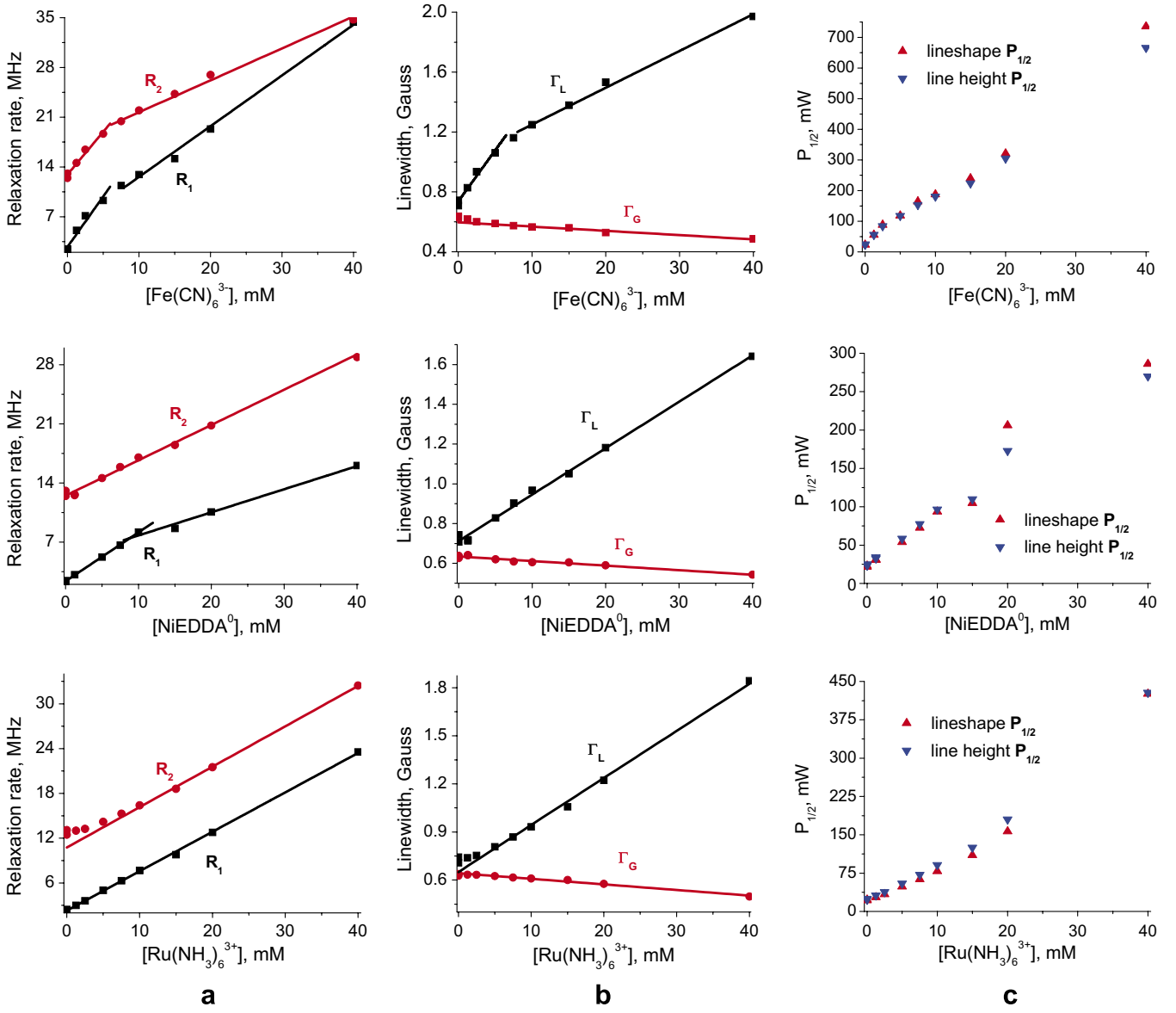

Fig. 11. MSL-PEG bead column results. Values plotted as in Fig. 6. $R_{20}/R_{10} = 3$ as evident in column (a). Bimodal R_1 plots for $Fe(CN)_6^{3-}$ and $NiEDDA^0$ in column (a) suggest coordination effects which limit collisional spin exchange past 10 mM. Initial linewidth changes are significant for the charged PRAs in column (b). $Fe(CN)_6^{3-}$ has the strongest relaxation on the system and $Ru(NH_3)_6^{3+}$ the weakest as expected for the positively charged environment. Note that nonlinearities in half-saturation power $P_{1/2}$ match between lineshape and lineheight fitting results in column (c). Here lineshape data is multiplied by 1.1, 1.25 and 1.3 in column (c) for added $Fe(CN)_6^{3-}$, $NiEDDA^0$ and $Ru(NH_3)_6^{3+}$, to match with data from lineheight, respectively.

square roots of $P_{1/2}$ changes from lineheight fitting. In the slow tumbling limit $R_2 \gg R_1$ making direct ratio of the $P_{1/2}$ changes the most accurate approximation. Lineshape fitting may be used to find the ratio between the changes in R_1 for such pairs across the whole range of cases, being less accurate that lineheight fitting only in the slow tumbling limit. We believe that it will be an important tool for accurate determination of voltage in intermediate cases where a label is floppy on a protein site.

4.4. Error between $P_{1/2}$ curves

$P_{1/2}$ curves derived from lineshape must be multiplied by constants from 1.0 for deuterated tempone to 1.4 for ASL-cys-allyl, with added $Co(CN)_6^{3-}$ or $Co(NH_3)_6^{3+}$ ions, to match those from lineheight, with specific examples in Figs. 6–12. The constant reveals an error that correlates with the degree of inhomogeneity in spectra. We attribute this to the absolute value of R_1 from lineheight fitting being more sensitive than the R_1 obtained from lineshape fitting to errors associated with discrete superhyperfine splitting and its averaging by setting the modulation amplitude close to peak-to-peak linewidth. Since our goal here has been to determine accurate relaxivities we are less concerned about the absolute value of R_1, which is not determined directly in lineheight measurements on proteins anyway.

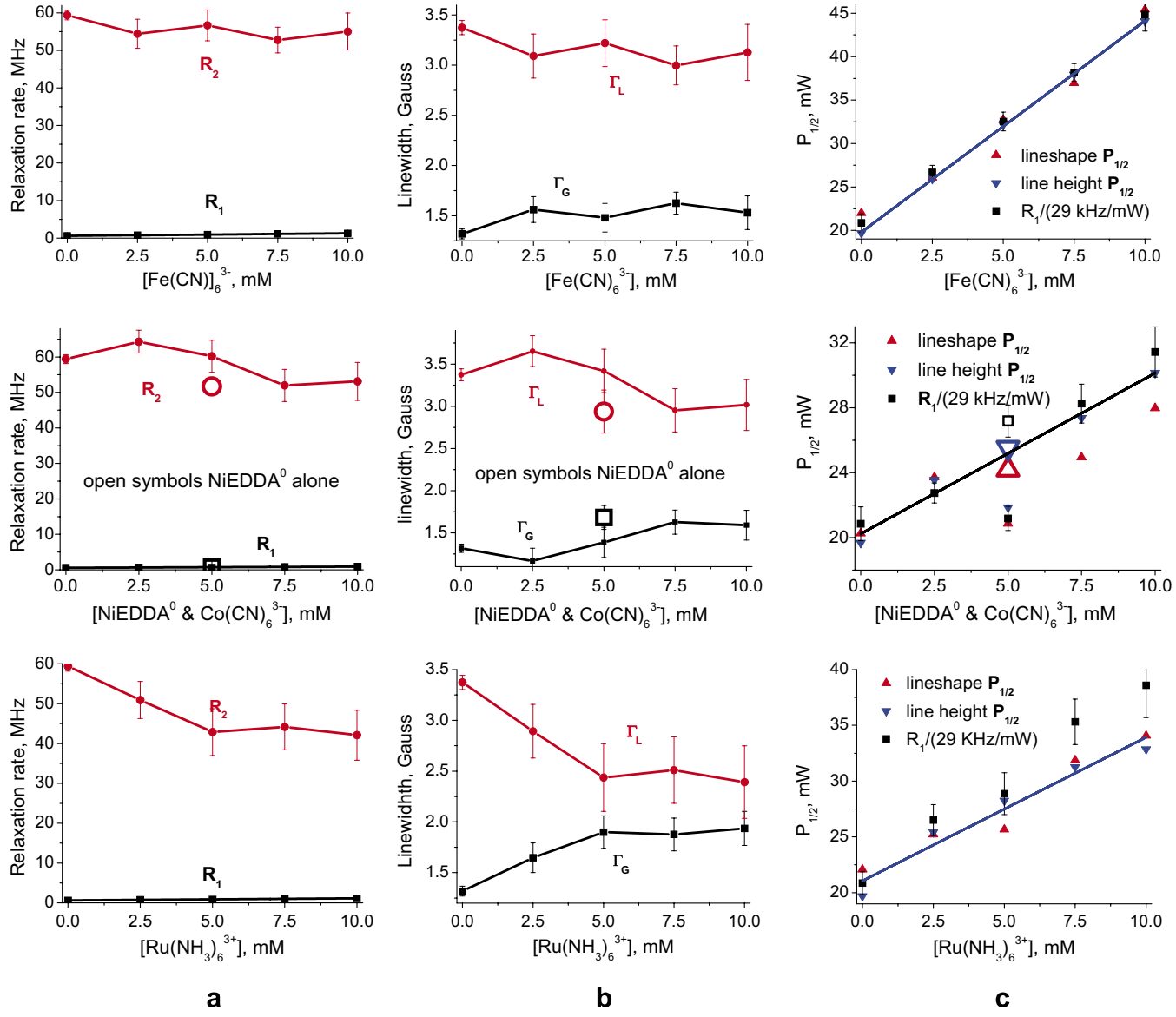

Fig. 12. ASL-S1 results. Values plotted as in Fig. 6. Here $R_{20}/R_{10} \approx 100$ in column (a). This rigidly labeled protein case is at the extreme limit for global lineshape fitting. $Fe(CN)_6^{3-}$ is the most accessible while $NiEDDA^0$ proves to be the least accessible based on the scatter in the $P_{1/2}$ plots of column (c). CrOx is even less accessible (results not shown). R_1 show a linear increase with added PRA in all cases in columns (a) and (c). $P_{1/2}$ curves in column (c) are linear and reflect R_1 enhancement as expected and lineshape $P_{1/2}$ values are increased by a factor of 1.1 in column (c) for an overall fit to line height values.

5. Conclusions

We have calibrated a set of fast-relaxing PRAs for voltage measurements on spin labeled proteins with conventional EPR. We found correction factors of 1.35 for $Fe(CN)_6^{3-}$ and 1.54 for $Ru(NH_3)_6^{3+}$, to account for their higher spin exchange rates with respect to $NiEDDA^0$. Using these correction factors, measured voltages for TEMPO-choline and carboxy-TEMPO lie within 1 mV of values calculated with Debye-Hückel theory. We validated the voltages measured with our PRAs on rabbit myosin S1 labeled at Cys707 with IASL, finding a match between measured voltages determined through lineheight fitting and those calculated based on the pK shift at Cys707 (thiol SH1) to about 1 mV. R_1 values were determined for small nitroxides from progressive saturation spectra through global lineshape fitting to perform these calibrations. The method and PRA set works even in the extreme case of a rigid label in a protein crevice as our measured voltages from lineshape and lineheight fitting on ASL-S1 show. We conclude that our calibrated set of PRAs can measure voltage with 1 mV accuracy for all nitroxides in buffer solution, from freely tumbling small molecules to spin-labeled proteins.

Acknowledgments

This work has been supported from grants to DDT from NIH (AR32961, GM27906). We are grateful to Karol Subczynski and Justyna Widomska in the National Biological

EPR Center in Milwaukee (NIH center Grant # EB001980) for assistance in R_1 measurements using saturation recovery. We thank Igor V. Negrashov for excellent programming assistance. We thank Yuri Nesmelov and Adam Burr for helpful discussions. Small molecule modeling was done in Fujitsu Cache™.

References

[1] B. Honig, A. Nicholls, Classical electrostatics in biology and chemistry, Science 268 (1995) 1144–1149.
[2] F. Fogolari, A. Brigo, H. Molinari, The Poisson–Boltzmann equation for biomolecular electrostatics: a tool for structural biology, Journal of Molecular Recognition 15 (2002) 377–392.
[3] J.L. Liao, D.N. Beratan, How does protein architecture facilitate the transduction of ATP chemical-bond energy into mechanical work? The cases of nitrogenase and ATP binding-cassette proteins, Biophysical Journal 87 (2004) 1369–1377.
[4] D.A. Stauffer, A. Karlin, Electrostatic potential of the acetylcholine binding sites in the nicotinic receptor probed by reactions of binding-site cysteines with charged methanethiosulfonates, Biochemistry 33 (1994) 6840–6849.
[5] A. Karlin, M.H. Akabas, C. Czajkowski, C. Kaufmann, D. Stauffer, M. Xu, Structures involved in binding, gating, and conduction in nicotinic acetylcholine receptors, Renal Physiology and Biochemistry 17 (1994) 184–186.
[6] S. Highsmith, K. Polosukhina, D. Eden, Myosin motor domain lever arm rotation is coupled to ATP hydrolysis, Biochemistry 39 (2000) 12330–12335.
[7] N. Sasaki, R. Ohkura, K. Sutoh, Dictyostelium myosin II mutations that uncouple the converter swing and ATP hydrolysis cycle, Biochemistry 42 (2003) 90–95.
[8] R.P. Feynmann, Forces in molecules, Physical Review 56 (1939) 340–343.
[9] H. Hellmann, Einfuhrung in die Quantenchemie 1937. F. Deuticke, Leipzig.
[10] J.S. Anderson, D.M. Lemaster, G. Hernandez, Electrostatic potential energy within a protein monitored by metal charge-dependent hydrogen exchange, Biophysical Journal 91 (2006) L93–L95.
[11] D.W. Urry, D.C. Gowda, S. Peng, T.M. Parker, Non-linear hydrophobic-induced p*K*a shifts: implications for efficiency of conversion to chemical energy, Chemical Physics Letters 239 (1995) 67–74.
[12] D.W. Urry, S. Peng, D.C. Gowda, T.M. Parker, Comparison of electrostatic and hydrophobic-induced p*K*a shifts in polypentapeptides: the lysine residue, Chemical Physics Letters 225 (1994) 97–103.
[13] M.J.E. Sternberg, F.R.F. Hayes, A.J. Russell, P.G. Thomas, A.R. Fersht, Prediction of electrostatic effects of engineering of protein charges, Nature 330 (1987) 86–88.
[14] R.L. Thurlkill, G.R. Grimsley, J.M. Scholtz, C.N. Pace, p*K* values of the ionizable groups of proteins, Protein Science 15 (2006) 1214–1218.
[15] K. Takamori, K.A. Kato, T. Sekine, Thiols of myosin. IV. ''Abnormal'' reactivity of S1 thiol and the conformational changes around S2 thiol, Journal of Biochemistry (Tokyo) 80 (1976) 101–110.
[16] Y.K. Shin, W.L. Hubbell, Determination of electrostatic potentials at biological interfaces using electron–electron double resonance, Biophyscial Journal 61 (1992) 1443–1453.
[17] J.L. Hecht, B. Honig, Y.K. Shin, W.L. Hubbell, Electrostatic potentials near-the-surface of DNA—Comparing theory and experiment, Journal of Physical Chemistry 99 (1995) 7782–7786.
[18] S. Highsmith, K. Duignan, K. Franks-Skiba, K. Polosukhina, R. Cooke, Reversible inactivation of myosin subfragment 1 activity by mechanical immobilization, Biophysical Journal 74 (1998) 1465–1472.
[19] J.E. Baker, I. Brust-Mascher, S. Ramachandran, L.E. LaConte, D.D. Thomas, A large and distinct rotation of the myosin light chain domain occurs upon muscle contraction, Proceedings of the National Academy of Sciences of the United States of America 95 (1998) 2944–2949.
[20] F. Fogolari, L. Ragona, S. Licciardi, S. Romagnoli, R. Michelutti, R. Ugolini, H. Molinari, Electrostatic properties of bovine beta-lactoglobulin, Proteins 39 (2000) 317–330.
[21] R.D. Vale, AAA proteins. Lords of the ring, Journal of Cell Biology 150 (2000) F13–F19.
[22] R.D. Vale, Switches, latches, and amplifiers: common themes of G proteins and molecular motors, Journal of Cell Biology 135 (1996) 291–302.
[23] A. Karlin, Scam feels the pinch, Journal of General Physiology 117 (2001) 235–238.
[24] M.N. Davies, C.P. Toseland, D.S. Moss, D.R. Flower, Benchmarking p*K*(a) prediction, BMC Biochemistry 7 (2006) 18.
[25] G. Kossekova, M. Miteva, B. Atanasov, Characterization of pyridoxal phosphate as an optical label for measuring electrostatic potentials in proteins, Journal of Photochemistry and Photobiology B. 32 (1996) 71–79.
[26] C. Christov, D. Ianev, A. Shosheva, B. Atanasov, pH-dependent quenching of the fluorescence of tryptophan residues in class A beta-lactamase from *E. coli* (TEM-1), Z Naturforsch [C] 59 (2004) 824–827.
[27] A.P. Winiski, M. Eisenberg, M. Langer, S. McLaughlin, Fluorescent probes of electrostatic potential 1 nm from the membrane surface, Biochemistry 27 (1988) 386–392.
[28] T. Ando, N. Kobayashi, E. Munekata (Eds.), in: H.S.a.G.H. Pollack (Ed.), Electrostatic Potential Around Actin, Advances in Experimental Medicine and Biology, vol. 332, 1993, pp. 361–376.
[29] T. Yamamoto, S. Nakayama, N. Kobayashi, E. Munekata, T. Ando, Determination of electrostatic potential around specific locations on the surface of actin by diffusion-enhanced fluorescence resonance energy transfer, Journal of Molecular Biology 241 (1994) 714–731.
[30] T.G. Wensel, C.F. Meares, Electrostatic properties of myoglobin probed by diffusion-enhanced energy transfer, Biochemistry 22 (1983) 6247–6254.
[31] T.G. Wensel, C.-H. Chang, C.F. Meares, Diffusion-enhanced lanthanide energy-transfer study of DNA-bound cobalt(III) bleomycins: comparisons of accessibility and electrostatic potential with DNA complexes of ethidium and acridine orange, Biochemistry 24 (1985) 3060–3069.
[32] R.H. Meltzer, W. Vila-Carriles, J.O. Ebalunode, J.M. Briggs, S.E. Pedersen, Computed pore potentials of the nicotinic acetylcholine receptor, Biophysical Journal 91 (2006) 1325–1335.
[33] R.H. Meltzer, E. Thompson, K.V. Soman, X.Z. Song, J.O. Ebalunode, T.G. Wensel, J.M. Briggs, S.E. Pedersen, Electrostatic steering at acetylcholine binding sites, Biophysical Journal 91 (2006) 1302–1314.
[34] R.H. Meltzer, M.M. Lurtz, T.G. Wensel, S.E. Pedersen, Nicotinic acetylcholine receptor channel electrostatics determined by diffusion-enhanced luminescence energy transfer, Biophysical Journal 91 (2006) 1315–1324.
[35] C.-L. Teng, R.G. Bryant, Spin relaxation measurements of electrostatic bias in intermolecular exploration, Journal of Magnetic Resonance 179 (2006) 199–205.
[36] G.I. Likhtenshtein, I. Adin, A. Novoselsky, A. Shames, I. Vaisbuch, R. Glaser, NMR studies of electrostatic potential distribution around biologically important molecules, Biophysical Journal 77 (1999) 443–453.
[37] G.I. Liktenshtein, Y.B. Grebenshchikov, T.V. Avilova, An investigation of the microrelief and conformational mobility of proteins by the ESR method, Molecular Biology (translated from Russian) 6 (1972) 67–76.

[38] Y. Lin, R. Nielsen, D. Murray, W.L. Hubbell, C. Mailer, B.H. Robinson, M.H. Gelb, Docking phospholipase A(2) on membranes using electrostatic potential-modulated spin relaxation magnetic resonance, Science 279 (1998) 1925–1929.
[39] Y.B. Grebenshchikov, G.I. Likhtenshtein, V.P. Ivanov, E.G. Rozantsev, Investigation of electrostatic charges in proteins by the paramagnetic probe method, Molecular Biology (translated from Russian) 6 (1972) 400–406.
[40] S. Canaan, R. Nielsen, F. Ghomashchi, B.H. Robinson, M.H. Gelb, Unusual mode of binding of human group IIA secreted phospholipase A(2) to anionic interfaces as studied by continuous wave and time domain electron paramagnetic resonance spectroscopy, Journal of Biological Chemistry 277 (2002) 30984–30990.
[41] G.I. Likhtenshtein, Spin Labeling Methods in Molecular Biology, Wiley, 1976.
[42] G.H. Addona, S.H. Andrews, D.S. Cafiso, Estimating the electrostatic potential at the acetylcholine receptor agonist site using power saturation EPR, Biochimica et Biophysica Acta 1329 (1997) 74–84.
[43] R.D. Nielsen, S. Canaan, J.A. Gladden, M.H. Gelb, C. Mailer, B.H. Robinson, Comparing continuous wave progressive saturation EPR and time domain saturation recovery EPR over the entire motional range of nitroxide spin labels, Journal of Magnetic Resonance 169 (2004) 129–163.
[44] J.S. Hyde, J.C.W. Chien, J.H. Freed, Electron–electron double resonance of free radicals in solution, Journal of Chemical Physics 48 (1968) 4211–4226.
[45] L.A. Dalton, J.-L. Monge, L.R. Dalton, A.L. Kwiram, Molecular and applied modulation effects in electron–electron double resonance III. Bloch equation analysis for inhomogeneous broadening, Chemical Physics 6 (1974) 166–182.
[46] J.S. Hyde, T. Sarna, Magnetic interactions between nitroxide free radicals and lanthanides or Cu^{2+} in liquids, Journal of Chemical Physics 68 (1978) 4439–4447.
[47] C. Altenbach, W. Froncisz, J.S. Hyde, W.L. Hubbell, Conformation of spin-labeled melittin at membrane surfaces investigated by pulse saturation recovery and continuous wave power saturation electron paramagnetic resonance, Biophysical Journal 56 (1989) 1183–1191.
[48] J. Pyka, J. Ilnicki, C. Altenbach, W.L. Hubbell, W. Froncisz, Accessibility and dynamics of nitroxide side chains in T4 lysozyme measured by saturation recovery EPR, Biophysical Journal 89 (2005) 2059–2068.
[49] Y.N. Molin, K.M. Salikhov, K.I. Zamaraev, Spin exchange, principles and applications in chemistry and biology, in: E.A. Goldanskii (Ed.), Springer series in chemical physics, Springer, 1980.
[50] A.V. Kulikov, G.I. Likhtenstein, The use of spin relaxation phenomena in the investigation of the structure of model and biological systems by the method of spin labels, Advances in molecular relaxation and interaction processes 10 (1977) 47–79.
[51] T.L. Hill, An Introduction to Statistical Thermodynamics, Dover, 1956.
[52] B.L. Bales, D. Willett, EPR investigation of the intermediate spin exchange regime, Journal of Chemical Physics 80 (1984) 2997–2999.
[53] D. Waysbort, G. Navon, NMR study of the nature of the second coordination sphere in aqueous solutions of ruthenium(III) hexaammine, Journal of Physical Chemistry 84 (1980) 674–678.
[54] D.F. Averill, J.I. Legg, D.L. Smith, Five-coordinate square-pyramidal chelate complexes of a novel tetradentate amino acid like ligand, Inorganic Chemistry 11 (1972) 2344–2349.
[55] D. Waysbort, G. Navon, Proton NMR and covalency parameters of ruthenium(III) hexaammine, Journal of Chemical Physics 59 (1973) 5585–5590.
[56] B.N. Figgis, P.A. Reynolds, Diffraction experiments and the theory of simple transition metal complexes, International Reviews in Physical Chemistry 5 (1986) 265–272.
[57] J. Cano, E. Ruiz, S. Alvarez, M. Verdaguer, Spin density distribution in transition metal complexes: some thoughts and hints, Comments on Inorganic Chemistry 20 (1998) 27–56.
[58] C. Altenbach, Accessibility of nitroxide side chains: absolute Heisenberg exchange rates from power saturation EPR, Biophysical Journal 89 (2005) 2103–2112.
[59] O.A. Anisimov, A.T. Nikitaev, K.I. Zamaraev, Y.N. Molin, Separation of exchange and dipole–dipole broadening on the basis of viscosity changes is ESR spectra, Theoretical and Experimental Chemistry (translated from Russian) 7 (1971) 556–559, originally 682-686.
[60] Y. Pontillon, A. Grand, T. Ishida, E. Lelievre-Berna, T. Nogami, E. Ressouche, J. Schweizer, Spin density of a ferromagnetic TEMPO derivative: polarized neutron investigation and ab initio calculation, Journal of Materials Chemistry 10 (2000) 1539–1546.
[61] L. Pauling, General Chemistry, Dover reprint edition, 1988.
[62] H. Taube, Substitution reactions of ruthenium ammines, Comments on Inorganic Chemistry 1 (1981) 17–31.
[63] P. Graceffa, J.C. Seidel, A reaction involving protein sulfhydryl groups, a bound spin-label, and $K_3Fe(CN)_6$ as a probe of sulfhydryl proximity in myosin, Biochemistry 19 (1980) 33–39.
[64] P.R. Bergethon, E.R. Simons, Biophysical Chemistry, Springer Verlag, 1990.
[65] M. Daune, Molecular Biophysics; Structures in Motion, Oxford University Press, 1999.
[66] C. Altenbach, S.L. Flitsch, G. Khorana, W.L. Hubbell, Structural studies of transmembrane proteins. 2. Spin Labeling of bacteriorhodopsin mutants at unique cysteines, Biochemistry 28 (1989) 7806–7812.
[67] C. Altenbach, A. Duncan, H. Greenhalgh, G. Khorana, W.L. Hubbell, A collision gradient method to determine the immersion depth of nitroxides in lipid bilayers: Application to spin-labeled mutants of bacteriorhodopsin, Proceedings of the National Academy of Science United States of America 91 (1994) 1667–1671.
[68] M. Sahlin, A. Graslund, A. Ehrenberg, Determination of relaxation times for a free radical from microwave saturation studies, Journal of Magnetic Resonance 67 (1986) 135–137.
[69] J.S. Hyde, W.K. Subczynski, Spin Label Oximetry, in: L.J.a.R.J. Berliner (Ed.), Biological Magnetic Resonance, Plenum, 1989.
[70] K.M. More, G.R. Eaton, S.S. Eaton, Determination of T1 and T2 by simulation of EPR power saturation curves and saturated spectra. Application to spin-labeled iron porphyrins, Journal of Magnetic Resonance 60 (1984) 54–65.
[71] A.M. Portis, Electronic structure of F centers: saturation of the electron spin resonance, Physical Review 91 (1953) 1071–1078.
[72] T.G. Castner, Saturation of the paramagnetic resonance of a V center, Physical Review 115 (1959) 1506–1515.
[73] B.L. Bales, Inhomogeneously broadened spin label spectra, in: Spin Labeling Theory and Applications, Plenum, 1989 (Chapter 2).
[74] C.P. Poole, Electron Spin Resonance. 2nd ed., Dover reprint of 1983 Wiley edition, 1996.
[75] B.H. Robinson, C. Mailer, A.W. Reese, Linewidth analysis of spin labels in liquids I. Theory and data analysis, Journal of Magnetic Resonance 138 (1999) 199–209.
[76] B.H. Robinson, C. Mailer, A.W. Reese, Linewidth analysis of spin labels in liquids II. Experimental, Journal of Magnetic Resonance 138 (1999) 210–219.
[77] J.S. Hwang, R.P. Mason, L.P. Hwang, J.H. Freed, Electron spin resonance studies of anisotropic rotational reorientation and slow tumbling in liquid and frozen media. III. Perdeuterated 2,2,6,6-tetramethyl-4-piperidone N-oxide and an analysis of fluctuating torques, Journal of Physical Chemistry 79 (1975) 489–511.
[78] D.A. Windrem, W.Z. Plachy, The diffusion-solubility of oxygen in lipid bilayers, Biochimica et Biophysica Acta 600 (1980) 655–665.
[79] J.S. Hyde, W.K. Subczynski, Simulation of ESR spectra of the oxygen-sensitive spin-label probe CTPO, Journal of Magnetic Resonance 56 (1984) 125–130.
[80] A.I. Smirnov, R.L. Belford, Rapid quantitation from inhomogeneously broadened EPR spectra by a fast convolution algorithm, Journal of magnetic Resonance, Series A 113 (1995) 65–73.

[81] D. Marsh, Experimental methods in spin-label spectral analysis, in: Spin Labeling Theory and Applications, Plenum, 1989 (Chapter 5).
[82] V.A. Barnett, D.D. Thomas, Resolution of conformational states of spin-labeled myosin during steady-state ATP hydrolysis, Biochemistry 26 (1987) 314–323.
[83] E.J. Shimshick, H.M. McConnell, Lateral phase separation in phospholipid membranes, Biochemistry 12 (1973) 2351–2360.
[84] R.G. Kooser, W.V. Volland, J.H. Freed, ESR relaxation studies on orbitally degenerate free radicals. I. Benzene anion and tropenyl, Journal of Chemical Physics 50 (1969) 5243–5257.
[85] T. Kirby, C.B. Karim, D.D. Thomas, Electron paramagnetic resonance reveals a large-scale conformational change in the cytoplasmic domain of phospholamban upon binding to the sarcoplasmic reticulum Ca-ATPase, Biochemistry 42 (2004) 5842–5852.
[86] G. Diakova, R.G. Bryant, The aqueous reference for ESR oximetry, Journal of Magnetic Resonance 178 (2006) 329–333.
[87] T.D. Yager, G.R. Eaton, S.S. Eaton, Metal-nitroxyl interactions. 12. Nitroxyl spin probes in the presence of tris(oxalato)chromate(III), Inorganic Chemistry 18 (1979) 725–727.
[88] Y. Hiratsuka, M. Eto, M. Yazawa, F. Morita, Reactivities of Cys707 (SH1) in intermediate states of myosin subfragment-1 ATPase, Journal of Biochemistry (Tokyo) 124 (1998) 609–614.
[89] C. Tanford, R. Roxby, Interpretation of protein titration curves. Application to lysozyme, Biochemistry 11 (1972) 2192–2198.
[90] D.A. Haas, C. Mailer, B.H. Robinson, Using nitroxide spin labels, Biophysical Journal 64 (1993) 594–604.
[91] S.N. Dobryakov, Y.S. Lebedev, Analysis of spectral lines whose profile is described by a composition of Gaussian and Lorentz profiles, Soviet Physics—Dolkady 13 (1969) 873–875.
[92] M.P. Eastman, R.G. Kooser, M.R. Das, J.H. Freed, Studies of Heisenberg spin exchange ESR spectra. I. Linewidth and saturation effects, Journal of Chemical Physics 51 (1969) 2690–2708.
[93] C.P. Poole, H.A. Farach (Eds.), Handbook of Electron Spin Resonance, American Institute of Physics, 1994.
[94] Bertini, I., Luchinat, C., Parigi, G., 1H NMRD profiles of paramagnetic aquo-complexes and metalloproteins, In: VanEldik, R., Bertini, I. (Eds.), Relaxometry of water-metal ion interactions, 2005, pp. 105–172.
[95] C.-L. Teng, H. Hong, S. Kihne, R.G. Bryant, Molecular oxygen spin-lattice relaxation in solutions measured by proton magnetic relaxation dispersion, Journal of Magnetic Resonance 148 (2001) 31–34.
[96] M.G. Lyapilina, E.I. Krylov, V.A. Sharov, Electron spectra and magnetochemical study of chromium oxalate hexahydrate and its complex compounds in hydrazine, Ahurnal Neorganicheskoi Khimii 20 (1975) 816–817.
[97] B.N. Figgis, J. Lewis, F.E. Mabbs, G.A. Webb, Magnetic properties of some Iron(III) and Ruthenium(III) low-spin complexes, Journal of the Chemical Society A, Inorganic Physical Theory (1966) 422–426.
[98] Chiarotti, Giulotto, Proton relaxation in water, Physical Review 93 (1954) 1241.
[99] N. Bloembergen, Proton relaxation times in paramagnetic solution, Journal of Chemical Physics 27 (1957) 572–573.
[100] N. Bloembergen, L.O. Morgan, Proton relaxation times in paramagnetic solutions. Effects of electron spin relaxation, Journal of Chemical Physics 34 (1961) 842–850.